Guanine-adenine interactions in DNA tetranucleotide cation radicals revealed by UV/vis photodissociation action spectroscopy and theory

Journal:	*Physical Chemistry Chemical Physics*
Manuscript ID	CP-ART-05-2020-002362.R1
Article Type:	Paper
Date Submitted by the Author:	26-Jun-2020
Complete List of Authors:	Liu, Yue; University of Washington, Department of Chemistry Huang, Shu; University of Washington, Department of Chemistry Turecek, Frantisek; University of Washington, Department of Chemistry

Guanine-adenine interactions in DNA tetranucleotide cation radicals revealed by UV/vis photodissociation action spectroscopy and theory

Yue Liu, Shu R. Huang and František Tureček*

Hydrogen-rich cation radicals $(GATT+2H)^{+\bullet}$ and $(AGTT+2H)^{+\bullet}$ represent oligonucleotide models of charged hydrogen atom adducts to DNA. These tetranucleotide cation radicals were generated in the gas phase by one-electron reduction of the respective $(GATT+2H)^{2+}$ and $(AGTT+2H)^{2+}$ dications in which the charging protons were placed on the guanine and adenine nucleobases. We used wavelength-dependent UV/Vis photodissociation in the valence-electron excitation region of 210-700 nm to produce action spectra of $(GATT+2H)^{+\bullet}$ and $(AGTT+2H)^{+\bullet}$ that showed radical-associated absorption bands in the near-UV (330 nm) and visible (400-440 nm) regions. Born-Oppenheimer molecular dynamics and density-functional theory calculations were used to obtain and rank by energy multiple (GATT+2H) dication and cation-radical structures. Time-dependent density functional theory (TD-DFT) calculations of excited-state energies and electronic transitions in $(GATT+2H)^{+\bullet}$ were augmented by vibronic spectra calculations at 310 K for selected low-energy cation radicals to provide match with the action spectrum. The stable product of one-electron reduction was identified as having a 7,8-dihydroguanine cation radical moiety, formed by intramolecular hydrogen atom migration from adenine N-1-H. The hydrogen migration was calculated to have a transition state with a low activation energy, $E_a = 96.5$ kJ mol^{-1}, and positive activation entropy, $\Delta S^{\ddagger} = 75$ J mol^{-1} K^{-1}. This allowed for a fast isomerization of the primary reduction products on the ion-trap time scale of 150 ms that was substantially accelerated by highly exothermic electron transfer.

Department of Chemistry, Bagley Hall, Box 351700, University of Washington, Seattle, WA 98195-1700, USA. E-mail: turecek@chem.washington.edu

[†]Electronic supplementary information (ESI) available: Tables S1–S12 and Fig. S1–S5, Scheme S1. See DOI: 10.1039/xxxx

1. Introduction

Ionization of DNA by photons or high-energy particles forms cation radicals that undergo fast electron and proton transfer as the two fundamental secondary chemical processes.[1] The electron transfer kinetics in oligonucleotide and DNA intermediates has been elucidated for a number of model systems using down stream analysis of radical products.[2-5] In contrast, proton transfer between the Watson-Crick nucleobase pairs in DNA cation radicals has been studied for a limited number of model systems in solution,[6-8] as well as by density-functional theory calculations.[9-15] The main difficulty with studying DNA cation radicals in the early stages following ionization stems from their high reactivity in the condensed phase. Deprotonation by solvent has been shown to occur on a microsecond time scale, forming mixtures of secondary neutral products even from ionized nucleobases,[16,17] while experimental data for cation radicals of oligonucleotides have been scarce. Hence, it is advantageous to generate and study transient intermediates, such as DNA cation radicals, in an inert environment of the rarefied gas phase.[18] Following this strategy, O'Hair and coworkers have generated the cation radical of the cytosine-guanine Watson-Crick pair and characterized it by infrared multiphoton dissociation (IRMPD) action spectroscopy.[19] This method relies on generating the pertinent ion in an ion trap, isolating it by the mass-to-charge ratio (*m/z*), and monitoring its photodissociation over a range of wavelengths.[20-22] The ion trap conditions, which are ultrahigh vacuum for ion-cyclotron resonance mass spectrometry, or low pressure (3 mTorr) of helium in quadrupole ion traps, provide an inert medium that prevents intermolecular reactions that plague condensed phase studies of highly reactive species. In addition, detection of photofragment ions by mass spectrometry provides a highly sensitive means of monitoring ion light absorption even at an extremely low optical thickness of the absorber.

We have combined the multistage capabilities of quadrupole ion traps with UV-Vis photodissociation (UVPD) action spectroscopy to generate and characterize cation radicals of all four DNA nucleobases[23-26] as well as adenosine[27] and guanosine nucleosides.[25] Our strategy for the generation of oligonucleotide cation radicals relies on dication precursors that are formed in the gas phase by electrospray ionization. This guarantees that the charges, in the form of added protons, are localized on separate nucleobases in the dication. The dications are partly discharged by electron transfer from a gaseous donor, typically by an ion-ion reaction with

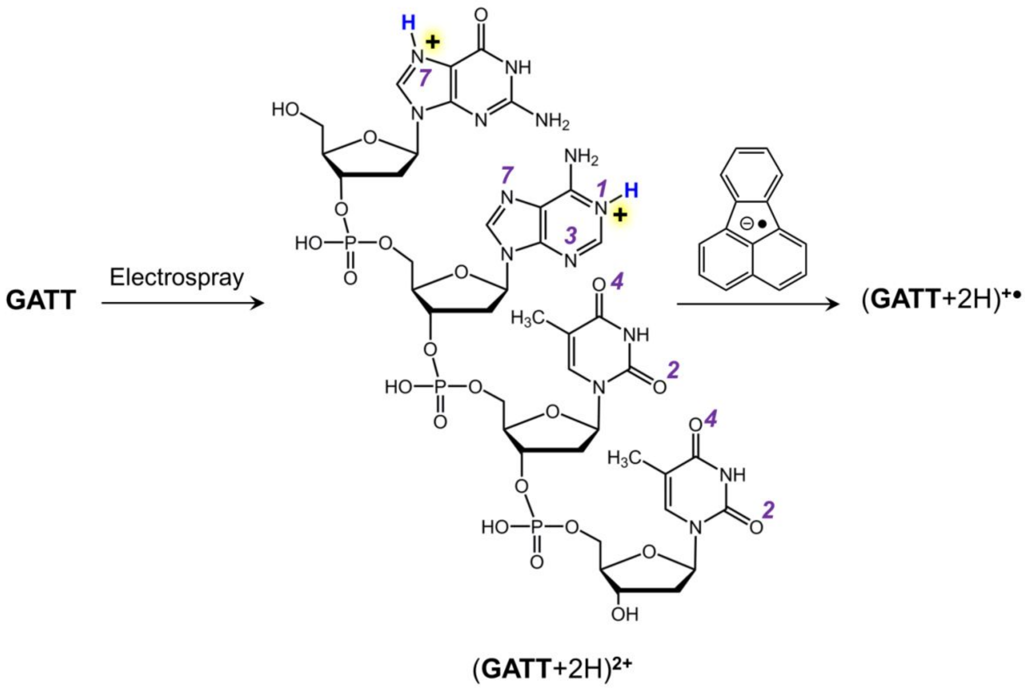

Scheme 1. Formation of $(GATT+2H)^{+\bullet}$ ions for UV-Vis action spectroscopy.

fluoranthene anion radical produced in an auxiliary ion source (Scheme 1).[28] Stable oligonucleotide cation radicals are selected by mass and studied by methods of tandem mass spectrometry, including UVPD action spectroscopy. The Scheme 1 reaction sequence, in which one-electron reduction follows protonation, can be viewed as a reversal of a pulse radiolysis sequence where addition of an electron is followed by protonation.[29,30] We have used one-electron reduction of dications to generate cation radicals from DNA dinucleotides AA,[31] GG, GC, CG,[32] and CC,[33] as well as tetranucleotides GATC and AGTC.[34] The previous studies have revealed that the cations and radicals that were located at different nucleobases in these oligonucleotides can undergo proton transfer between the nucleobases in a manner which depends on the nucleobases, their sequence, and oligonucleotide cation radical conformation. Here, we address the question of nucleobase cation-radical interaction in tetranucleotides GATT and AGTT. Because of the very different gas-phase basicities of G and A on one hand and T on the other,[35] these sequences are suitable for steering protonation towards the G and A nucleotides while preserving the conformational complexity of the dications and their cation-radical analogues. We wish to show that despite their low basicity, the thymine nucleotides engage in extensive hydrogen bonding interactions and thus have an effect on the conformational properties of the tetranucleotide cation radicals that affects proton transfer kinetics.

2. Experimental section

2.1. Materials

DNA tetranucleotides GATT and AGTT were purchased from Integrated DNA Technologies (Coralville, IA) and used as received.

2.2. Methods

Mass spectra were measured on a modified Bruker amaZon Speed 3D ion trap mass spectrometer (Bruker Daltonik, Bremen, Germany) equipped with an auxiliary ion source for electron transfer dissociation (ETD) and coupled to a laser.[36] The tetranucleotides were dissolved in 50:50:1 acetonitrile-water-acetic acid at 10-20 μM concentrations and electrosprayed into the ion trap. The doubly charged ions were partially reduced by ion-ion reactions with fluoranthene anion radicals at a 150-ms reaction time. The resulting cation radicals were again selected by mass in the ion trap and probed by laser photodissociation. An EKSPLA NL301G Nd-YAG laser (Altos Photonics, Bozeman, MT, USA) provided a beam at 20 Hz frequency and 3- to 6-ns pulse width. The photon pulses were treated by a PG142C unit (Altos Photonics, Bozeman, MT, USA) to enable wavelength tuning in the range of 210-700 nm, as reported previously.[37-39] The laser pulse energies were measured at each experimental wavelength using an EnergyMax-USB J-10MB energy sensor (Coherent Inc., Santa Clara, CA, USA) and used to normalize the action spectra according to the number of photons per pulse.

2.3 Calculations

Precursor $(GATT+2H)^{2+}$ dication structures were obtained for all 18 theoretical combinations of protomers in which protons were placed in the basic positions on different nucleobases, which were N-7 on G, N-1 or N-3 on A, and O-2 or O-4 on T3 and T4. Born−Oppenheimer molecular dynamics (BOMD) calculations were used to obtain 20 ps trajectories at 410−610 K using the Berendsen thermostat algorithm,[40] with the semiempirical all-valence-electron PM6 method[41] supplemented with corrections for dispersion and hydrogen bonding interactions, PM6-D3H4.[42] These calculations were run by MOPAC[43] under the Cuby4 platform,[44] as described previously.[33] Selected low-energy conformers from the BOMD runs of each protomer were reoptimized by density functional theory (DFT) calculations using the B3LYP[45] and ωB97X-D,[46] hybrid functionals with the 6-31+G(d,p) basis set. The B3LYP calculations provided harmonic frequencies that were used to calculate ion enthalpies and entropies at the ion trap temperature (310 K). The ωB97X-D calculations provided the electronic terms. The combined electronic, enthalpy, and entropy terms were combined to produce free energies that were used to rank conformers of each protomer. In addition, solvation energies in water were calculated with ωB97X-D/6-31+G(d,p) using the polarizable continuum model.[47] The lowest-free-energy gas-phase ions in each group were used for the selection of protomers in the charge-reduced $(GATT+2H)^{+\bullet}$ cation radicals. Cation-radical structures were optimized by B3LYP and M06-2X[48] calculations with the 6-31+G(d,p) basis set that were run within the spin unrestricted formalism. Single-point energies were calculated with M06-2X/6-311++G(2d,p) on the M06-2X/6-31+G(d,p) optimized geometries. Atomic spin densities were calculated using the natural population analysis[49] of the M06-2X/6-31+G(d,p) wave functions.

We selected UM06-2X/6-31+G(d,p) for time-dependent DFT calculations[50] of an extensive set of vertical and vibronic transitions in the cation radicals. This selection was based on our previous TD-DFT calculations that were benchmarked against high-level equation-of-motion coupled clusters (EOM-CCSD) calculations.[25,26] Vertical excitations were calculated for 90-145 excited states to probe all transitions within the experimentally studied region of 210-700 nm. The excitation wavelengths and oscillator strength are compiled in Supporting Tables S1-S11. To calculate vibronic excitations, we used 300 Boltzmann-ranked ground-state configurations that were generated by the Newton X program[51] from the B3LYP/6-31+G(d,p) calculated harmonic normal modes of each cation radical at 310 K and submitted for TD-DFT calculations. Because of the size of the tetranucleotide cation radicals and their open-shell nature we used a limited number of 10 excited electronic states in these vibronic TD-DFT calculations. All the electronic structure calculations were performed with the Gaussian 16 (revision A.03) suite of programs.[52] Rice-Ramsperger-Kassel-Marcus calculations[53] were run with a QCEP program[54] that was recompiled for Windows 7.[55] The calculations were performed in the 167-830 kJ mol^{-1} energy range with 2.092 kJ mol^{-1} (0.5 kcal mol^{-1}) steps and with a direct count of quantum states for the 393 and 392 normal vibrational modes in the reactant and transition state, respectively. Rotations were treated adiabatically, and the microcanonical $k(E,J,K)$ rate constants were Boltzmann-averaged over the population of rotational states at 310 K. Transition state theory calculations used the standard formula with the M06-2X/6-311++G(2d,p) activation energies and partition functions for the reactants and transition state that were based on B3LYP/6-31+G(d,p) normal-mode vibrational analysis and principal moments of inertia.

3. Results and discussion

3.1. Ion formation and characterization

Electrospray ionization of the GATT and AGTT tetranucleotides produced doubly charged ions, $(GATT+2H)^{2+}$ and $(AGTT+2H)^{2+}$, respectively, at *m/z* 595 (Scheme 1), that upon ion-ion reaction with fluoranthene anions formed the respective cation radicals, $(GATT+2H)^{+\bullet}$ and $(AGTT+2H)^{+\bullet}$, at *m/z* 1190 (Fig. 1a,b). One-electron reduction was accompanied by very little dissociation, resulting in a clean and efficient generation of the cation radicals. Likewise, proton transfer to the reagent anion, which is a common side reaction in ETD,**[28]** was minimal as evidenced by the low relative intensity of the $(GATT+H)^{+}$ and $(AGTT+H)^{+}$ ions at *m/z* 1189 (Fig. 1a,b insets).

The tetranucleotide cation radicals were selected by mass and investigated by collision-induced dissociation (CID-MS^3) to identify the fragment ions that may be suitable as detection channels for action spectroscopy. CID of $(GATT+2H)^{+\bullet}$ resulted in loss of water, adenine, and guanine nucleobases, forming cation-radical fragment ions at *m/z* 1172, 1055, and 1039, respectively (Fig. 2a). The main dissociations were backbone cleavages forming the 3'-terminal fragment ions $\boldsymbol{w}_3^+$, z_3^+, and $\boldsymbol{w}_2^+$ at *m/z* 940, 842, and 627, respectively (Fig. 2a). These were formed by loss of neutral radical fragments from the 5'-terminus and corresponded to even-electron ions. The backbone dissociations of this tetranucleotide cation radical were analogous to standard DNA ion fragmentations (for the DNA fragment ion nomenclature see ref.**[56,57]**), as also reported for other tetranucleotides.**[34]** UVPD at 250 nm of $(GATT+2H)^{+\bullet}$ produced fragment ions that were analogous to those from CID. The main difference was a diminished loss of guanine (*m/z* 1039) upon UVPD (Fig. 2b) compared to CID.

CID-MS^3 of $(AGTT+2H)^{+\bullet}$ (Fig. 3a) resulted in dissociations that differed from those of $(GATT+2H)^{+\bullet}$. Loss of 5'-terminal adenine (*m/z* 1055) was more abundant than loss of guanine (*m/z* 1039), pointing to the effect of the nucleobase position in the sequence. The dominant backbone cleavage between A and G led to the 3'-terminal $(\boldsymbol{w}_3+H)^{+\bullet}$ cation radical at *m/z* 957 (Fig. 3) that retained both the charging proton and the reduced hydrogen atom. However, the majority of backbone fragment ions from $(AGTT+2H)^{+\bullet}$ retained the 5'-terminus, such as the $\boldsymbol{d}_3^+$

(*m/z* 965), $(\boldsymbol{a}_3\text{+H})^{+\bullet}$ (*m/z* 866), and $\boldsymbol{d}_2^{+}$ (*m/z* 661) ions. In addition, we observed fragment ions at *m/z* 1007 and 1019 that can be formed by cross-ring dissociations in the T4 nucleotide and elimination of (T + H_2O + CO) for the former, and (T + C_3H_6O) for the latter fragment ion. These fragment ions are labeled with **xx** in the Fig. 3a spectrum. UVPD-MS^3 at 250 nm of $(\text{AGTT+2H})^{+\bullet}$ showed fragment ions that were similar to those from CID. Noteworthy is the enhanced formation on UVPD of the *m/z* 412 fragment ion. This can be formed from the $\boldsymbol{d}_2^{+}$ ion by consecutive eliminations of guanine (*m/z* 510) and phosphoric acid, resulting in an ion of the ($\boldsymbol{a}_2$ – G) type (Fig. 3b).

3.2. Action spectra

Wavelength-dependent photodissociation of $(\text{GATT+2H})^{+\bullet}$ was monitored at the main dissociation channels, *m/z* 1172, 1039, 940, 842, 716, and 627. The overall spectrum profile (Fig. 4a) is based on the sum of photofragment ion intensities. The action spectrum showed four distinct bands with maxima at 445, 330, 270, and 220 nm. These were all represented in the major mass-resolved photodissociation channels for the $\boldsymbol{w}_3^{+}$, $\boldsymbol{w}_2^{+}$, and $(z_3\text{-T})^{+}$ fragment ions (Fig. 4b,c). The channel for loss of G (*m/z* 1039) showed a stronger absorption band at 210-230 nm, and a slight shift of the near-UV band maximum from 330 nm to 350 nm (Fig. 4c). The bands above 300 nm can be assigned to radical chromophores, because neither nucleosides nor nucleoside gas-phase ions with closed electron shells absorb light above 300 nm.[58-60]

The action spectrum of $(\text{AGTT+2H})^{+\bullet}$ showed bands with maxima at 430, 330, 270, and 220 nm (Fig. 5a). The apparent split in the 270-nm band in the summed spectrum was caused by the slightly shifted maxima for the major contributing channels at *m/z* 957 and *m/z* 627 that appeared at ca. 260 and 275 nm, respectively (Fig. 5b). The major contributors to the 220-nm band were the *m/z* 1172, 965, and 866 channels (Fig. 5c). Overall, the action spectra of the $(\text{AGTT+2H})^{+\bullet}$ and $(\text{GATT+2H})^{+\bullet}$ sequence variants showed very similar overall absorption bands, indicating similar chromophores in these cation radicals.

3.3. Ion structures

To interpret the action spectra and assign structures to the cation radicals we carried out a detailed computational analysis of prototropic isomers of $(\text{GATT+2H})^{2+}$ precursor ions and $(\text{GATT+2H})^{+\bullet}$ cation radicals. Because of the large number of structures to be considered (*vide* *infra*) and the size and open-shell nature of the cation-radicals, we limited our analysis to the GATT set. On the basis of the low gas-phase basicity of thymine**[35]**, we presumed that double protonation by electrospray would primarily affect the more basic guanine and adenine nucleobases. Nevertheless, this assumption need not be satisfied in more complex systems, such as tetranucleotides, where internal hydrogen bonding may result in thymine protonation. Therefore, we carried out an extensive analysis of structures and energies of all 18 dication protomers. Based on the previous studies of topical gas-phase basicities of adenine,**[61-63]** guanine,**[64-68]** and thymine**[69]** we selected the N-1 and N-3 positions in adenine, N-7 in guanine, and O-2 and O-4 positions in thymine residues as the most probable protonation sites. The protomers are labeled according to the protonation sites, e.g. **G7A1** for the G-N-7, A-N-1 protomer and likewise for the others. For the nucleobase ring numbering, see Scheme 1. Several low-energy conformers of each of the 18 dication protomers were identified by Born-Oppenheimer molecular dynamics followed by full geometry optimization with DFT, as detailed in Section 2.3. Since the dications were produced from electrospray droplets in the presence of solvent, we also obtained relative free energies including solvation energies in water that were approximated using the polarizable continuum model.**[47]** According to our previous experience,**[32]** the ranking of relative energies of ions solvated by water and acetonitrile were very similar for both solvents, and so water solvation was deemed sufficient to capture the solvent effects in water-acetonitrile mixtures used in electrospray. The dication relative free energies are summarized in Table 1, the optimized structures of selected low-energy isomers are shown in Fig. 6.

The Table 1 data indicated that conformers of the G-7, A-1-protonated tautomer represented the lowest-energy structures of the $(GATT+2H)^{2+}$ dications. The lowest ΔH_0 conformer (**G7A1a**) displayed a highly folded globular conformation in which the protonated guanine was hydrogen-bonded to both neutral thymine nucleobases and the 3'-OH group (Fig. 6). Despite the extensive H-bonding, the G-7 and A-1 protons in **G7A1a** were positioned on the opposite faces of the ion at a 11.1 Å distance to minimize Coulomb repulsion. Two other low-energy conformers with the same protonation sites were represented by **G7A1b**, and **G7A1c**. The second lowest-energy conformer (**G7A1b**) had an extended geometry with the protonated guanine and T-3 on the opposite sides while the protonated adenine and T-4 were tightly hydrogen bonded (Fig. 6). This conformation allowed for a higher entropy of **G7A1b** that decreased its ΔG_{310} relative to **G7A1a** to 1.7 kJ mol^{-1} (Table 1). The other conformer, **G7A1c**, showed H-bonding between the protonated guanine and adenine nucleobases, which developed a further H-bond to T-3 (Figure 6). This conformation was particularly stabilized by solvation to become the global free energy minimum of (GATT+2H)$^{2+}$ ions solvated by water. In general, however, the energy differences between these conformers were small and well within the typical accuracy of the DFT calculations (estimated at ±10 kJ mol^{-1}) to allow any of these to be represented among the gas phase dications.

Out of the other tautomers, the G-7, A-3 and G-7, T-2 protonated ions, **G7A3a** and **G7T3-2**, respectively, had gas-phase free energies within 20 kJ mol^{-1} of **G7A1a**, while being disfavored by solvation (Table 1). The chief stabilizing structure feature of gas-phase **G7A3a** was the strong hydrogen bond of N-3–H to the proximate phosphate oxygen at 1.917 Å that allosterically enhanced H-bonding between the T4 O-2 and the phosphoester O-H at 1.588 Å (Fig. 6). Noteworthy is the backbone hydrogen bonding of the phosphate groups that formed the core of the **G7A3a** conformation (Fig. 6). Likewise, T3 protonation in **G7T3-2** was stabilized by a strong H-bond between T3 O-2-H and T4 O-2 at 1.450 Å, and the conformation was further reinforced by several phosphate H-bonds (Fig. 6). The ranges of conformer gas-phase free energies for all 18 (GATT+2H)$^{2+}$ tautomers are shown in Fig. S1 (Supporting Information). The data indicated that only the **G7A1**, **G7A3**, and **G7T3-2** tautomers had conformations that were within an energy range allowing their formation by proton-transfer under equilibrium conditions.

Several low-energy precursor dications (Table 1) representing different conformers of the **G7A1**, **G7A3**, **G7T3-2** tautomers were used as initial structures for electron attachment to obtain optimized structures and relative energies of (GATT+2H)$^{+\bullet}$ cation radicals (Table 2). Nucleobase reduction resulted in the formation of an adenine radical (**G7rA1**) from the **G7A1a** dication, while the other dication conformers yielded guanine based radicals **rG7A1a** and **rG7A1b** of similar relative energies (Table 2, Fig. 7). Since DFT calculations provide the ground electronic states of the cation-radicals, the site of reduction reflects the relative ion-electron recombination energies of the protonated nucleobases, whereby the site with the larger recombination energy was reduced to form the ground electronic state of the cation radical. This is illustrated by electron attachment to **G7A3a** that was accompanied by a phosphate proton migration, producing a thymine radical **G7rT3** in which the protonated guanine and adenine ring retained charge, the latter in a zwitterionic pair with a phosphate anion (Fig. 7). Electron attachment to thymine-protonated dications resulted in the formation of thymine radicals, such as **G7rT4** and **A1rT3** (Fig. 7). The Table 2 data further indicated that thymine radicals **G7rT3** and **G7rT4** were thermodynamically more stable than the adenine and guanine radicals of the **G7rA1** and **rG7A1** type.

3.4. Action spectra assignment

We used TD-DFT calculations to investigate excited electronic states in the above-discussed cation radicals with the goal of assigning the experimental action spectrum. However, none of the several cation-radical structures produced by electron attachment gave an absorption spectrum that would match the experiment (Fig. S2). The low-energy adenine-based (**G7rA1**, Fig. S2a, Table S1) and guanine-based radicals (**rG7A1a**, **rG7A1b**, Fig. S2b,c, Tables S2, S3) were calculated to have absorption bands for transitions to the ***B-D*** excited states at 550-600 nm that, however, were absent in the action spectrum. The low-energy thymine-based radicals (**G7rT3**, **G7rT4**, Fig. S2d,e, Tables S4, S6) had only extremely weak bands above 350 nm, which contradicted the action spectrum that showed distinct bands with maxima at 330 and 450 nm. We calculated TD-DFT absorption spectra of several other, higher-energy, radicals, but these revealed no match with the action spectrum either.

The mismatch of the calculated and action spectra indicated that the species produced by electron transfer did not retain the initially formed nucleobase radical chromophores of hydrogen atom adducts $(A+H)^\bullet$, $(G+H)^\bullet$, or $(T+H)^\bullet$. In particular, the UV-Vis action spectrum of a charge-tagged $(A+H)^\bullet$ radical has recently been reported to display a dominant band at 320 nm,[27] which is only weakly represented in the action spectrum of $(GATT+2H)^{+\bullet}$. According to previous studies of DNA di- and tetranucleotide radicals, the 330 and 450 nm bands in the action spectra could be indicative of 7,8-dihydroguanine[32] or 7,8-dihydroadenine cation radicals[31] produced by intramolecular hydrogen migration. To pursue this line of thought, we generated several cation-radical structures having the 7,8-dihydroguanine and 7,8-dihydroadenine motifs and found them to be substantially more stable than **G7rA1** (Table 2). The lowest energy isomers were 7,8-dihydroguanine cation radicals **rG78a**, **rG78b**, and **rG78c**, 7,8-dihydroadenine cation radical **rA78**, and the distonic adenine radical **G7rA8**, which retained the charging proton at guanine N-7 (Fig. 8). The energy data in Table 2 indicated that hydrogen atom migration to the C-8 positions in both guanine and adenine was substantially exothermic, providing the driving force for the isomerization. The relevant structures of the reactants, products, and transition state (TS) are shown in Scheme 2.

The absorption properties of a number of isomers potentially arising from isomerization were examined by TD-DFT spectra. Among these we found two conformational isomers, **rG78a** and **rG78b** (Fig. 9a,b), whose calculated absorption spectra showed approximate match with the action spectrum in the near UV and visible region. In particular, the spectrum of **rG78b** displayed bands with maxima at 394 and 330 nm due to transitions to the respective ***B*** and ***D*** excited states whereas the ***A*** and ***C*** states were silent. The spectrum of **rG78a** showed bands at 381 and 335 nm due to transitions to the respective ***A*** and ***C*** excited states. These two ions were selected for calculations of vibronic spectra of thermal ions at 310 K that included 10 lowest excited states, covering the critical wavelength range above 300 nm to be matched with the action spectrum. Covering a broader range of excited states in 300 vibrational configurations was unfeasible for these large open-shell systems of 1797 basis functions (3003 primitive gaussians). The 310-500 nm bands in the vibronic spectrum of **rG78b** showed an excellent match with the 330 and 445 nm bands in the action spectrum, as shown by the overlaid band profiles (Fig. 9b). The vibronic spectrum of **rG78a** (Fig. 9a) displayed a substantial dispersion and red shift of the 381 nm band due to ground state vibrations that resulted in a decreased match with the bands in the action spectrum. We note that the TD-DFT spectra of the other low-energy isomers (Fig. S3) provided a much less satisfactory match by either showing bands that were absent in the action spectrum, or conversely lacking some action spectrum bands. Based on the vibronic spectra and favorable relative energy, we assign the action spectrum to **rG78b** as the dominant component of cation radials formed by electron transfer to $(GATT+2H)^{2+}$ dications. Because of the broad bands in the action spectrum and ensuing limited wavelength resolution, we cannot exclude the presence of minor components that would overlap with **rG78b** and be compatible with the $(GATT+2H)^{+\bullet}$ relative energies.

3.5. Excited state molecular orbital analysis

The nature of the electronic excitations in **rG78b** and **rG78a** was examined by molecular orbital analysis that revealed further differences. The lowest-energy excitation (***A*** state, $\Delta E = 2.98$ eV) in **rG78b** was dipole disallowed (oscillator strength $f = 0.0006$) and was not expected to give rise to a band in the spectrum. This pertinent excitation involved an internal electron transition to the semi-occupied molecular orbital SOMO, (MO310β) that displayed substantial components of charge transfer from adenine to guanine. The ***B*** state, corresponding to the 392 nm band, also involved excitation within the β-electron manifold of π_z orbitals on guanine (MO304β → MO310β, Fig. 10, left panel). The ***D*** state, corresponding to the 330-nm band, was realized by an excitation from the SOMO (MO310α) to the virtual orbital space with a major component of MO312α. Interestingly, this transition involved substantial charge transfer from the adenine ring to the guanine radical (Fig. 10). In contrast, the lowest-energy transition leading to the ***A*** state in **rG78a**, which was represented by the 381-nm band, was a pure charge transfer from the thymine π-electron system (MO303β) to the SOMO on adenine (MO310β) that did not directly involved the guanine cation-radical. The substantial thermal broadening of the corresponding band (Fig. 10b, right panel) is understandable, because thermal motion in the ion affects the distance and mutual orientation of the adenine and thymine ring, thus affecting the dipole coupling for the electron transition. The next transition in this wavelength region (335 nm) was to the ***C*** state and involved π_z orbitals on guanine (MO310α → MO311α, Fig. 10).

3.6. GATT isomerization, dissociation energies and kinetics

The action spectra and energy analysis indicated that isomerization of **G7rA1** proceeded upon electron transfer and was 78 kJ mol^{-1} exothermic (by ΔH_0) when forming the **rG78b** cation radical (Scheme 2). The energy associated with the electron transfer reaction, $\Delta H_{rxn} < 0$, was estimated from eq 1, which can be equivalently described by heats of formation (ΔH_f, eq 2) or recombination energies (eq 3), where RE < 0 is the recombination energy of the **G7A1a** dication, and EA is the electron affinity of fluoranthene. Eq 2 and 3 in part rely on our previous finding that electron transfer from fluoranthene anion produces the neutral molecule in the ground singlet electronic state.[70]

$$(\mathbf{G7A1a})^{2+} + [\text{fluoranthene}]^{-\bullet} \rightarrow (\mathbf{G7rA1})^{+\bullet} + \text{fluoranthene} \quad (1)$$

$$\Delta H_{rxn} = \Delta H_f(\text{fluoranthene}) + \Delta H_f(\mathbf{G7rA1})^{+\bullet} - \Delta H_f(\text{fluoranthene})^{-\bullet} - \Delta H_f(\mathbf{G7A1a})^{2+} \quad (2)$$

$$\Delta H_{rxn} = \text{RE}(\mathbf{G7A1a})^{2+} + \text{EA}(\text{fluoranthene}) \quad (3)$$

We used the calculated RE for the lowest energy dications, –RE = 586, 589, and 552 kJ mol^{-1} for **G7A1a**, **G7A1b**, and **G7A1c**, respectively, and the EA of fluoranthene (EA = 82 kJ mol^{-1})**[34]** to estimate the electron transfer energy as 470-507 kJ mol^{-1}. This excess energy was supposed to be partitioned between (GATT+2H)$^{+\bullet}$ and the fluoranthene molecule in the ratio of their rovibrational heat capacities, giving an initial vibrational excitation in (GATT+2H)$^{+\bullet}$ as E_{exc} = 504 × 68.5/(68.5+10.7) = 436 kJ mol^{-1}. The internal energy distribution in the cation radical produced by electron transfer, $P(E)$, was expressed as a convolution of the precursor ion thermal energy at 310 K and the E_{exc} (Fig. 11a). RRKM rate constants $k(E)$ were calculated using the M06-2X/6-311++G(2d,p) energy for **TS1** (93 kJ mol^{-1}, Table 2) and convoluted with the $P(E)$ (Fig. 11b), to estimate the population-weighed rate of isomerization, k_{isom} (eq. 4), for the isomerization: **G7rA1** → **TS1** → **rG78b**.

$$k_{isom} = \int_{E_{TS}}^{\infty} k(E)P(E)dE \tag{4}$$

This result, $k_{\mathrm{isom}} = 9.6 \times 10^{6}$ s^{-1}, indicated that **G7rA1** would have a 72 ns half-life and therefore should isomerize completely on the time scale of the measurement (0.15 s). A complicating factor in these rate estimates was the collisional cooling of the internally hot ions under the conditions of 3 mTorr He in the ion trap. While the collision rate can be estimated from the He pressure and the calculated collision cross section, the collision energy transfer and its dependence on the ion internal energy were unknown. We have previously addressed this problem by expressing collisional cooling by competitive kinetics,**[34,70]** to solve eq. 5-8 for a range of cooling rate constants k_{cool}. The mole fraction of the **rG78b** isomerization product ($x_{\boldsymbol{rG78b}}$) is expressed by eq. 9:

$$-\frac{d[\boldsymbol{G7rA1}]_{hot}}{dt} = -(k_{isom} + k_{cool})[\boldsymbol{G7rA1}]_{hot} \tag{5}$$

$$\frac{d[\boldsymbol{rG78b}]}{dt} = k_{isom}[\boldsymbol{G7rA1}]_{hot} \tag{6}$$

$$\frac{d[\boldsymbol{G7rA1}]_{cool}}{dt} = k_{cool}[\boldsymbol{G7rA1}]_{hot} \tag{7}$$

$$x_{\boldsymbol{G7rA1}} = [\boldsymbol{G7rA1}]_{hot} + [\boldsymbol{G7rA1}]_{cool} \tag{8}$$

$$x_{\boldsymbol{rG78b}} = \int_{E_{TS}}^{\infty} \frac{k_{isom}(E)}{k_{isom}(E) + k_{cool}} \{1 - e^{-(k_{isom}(E) + k_{cool})t}\} P(E)dE \tag{9}$$

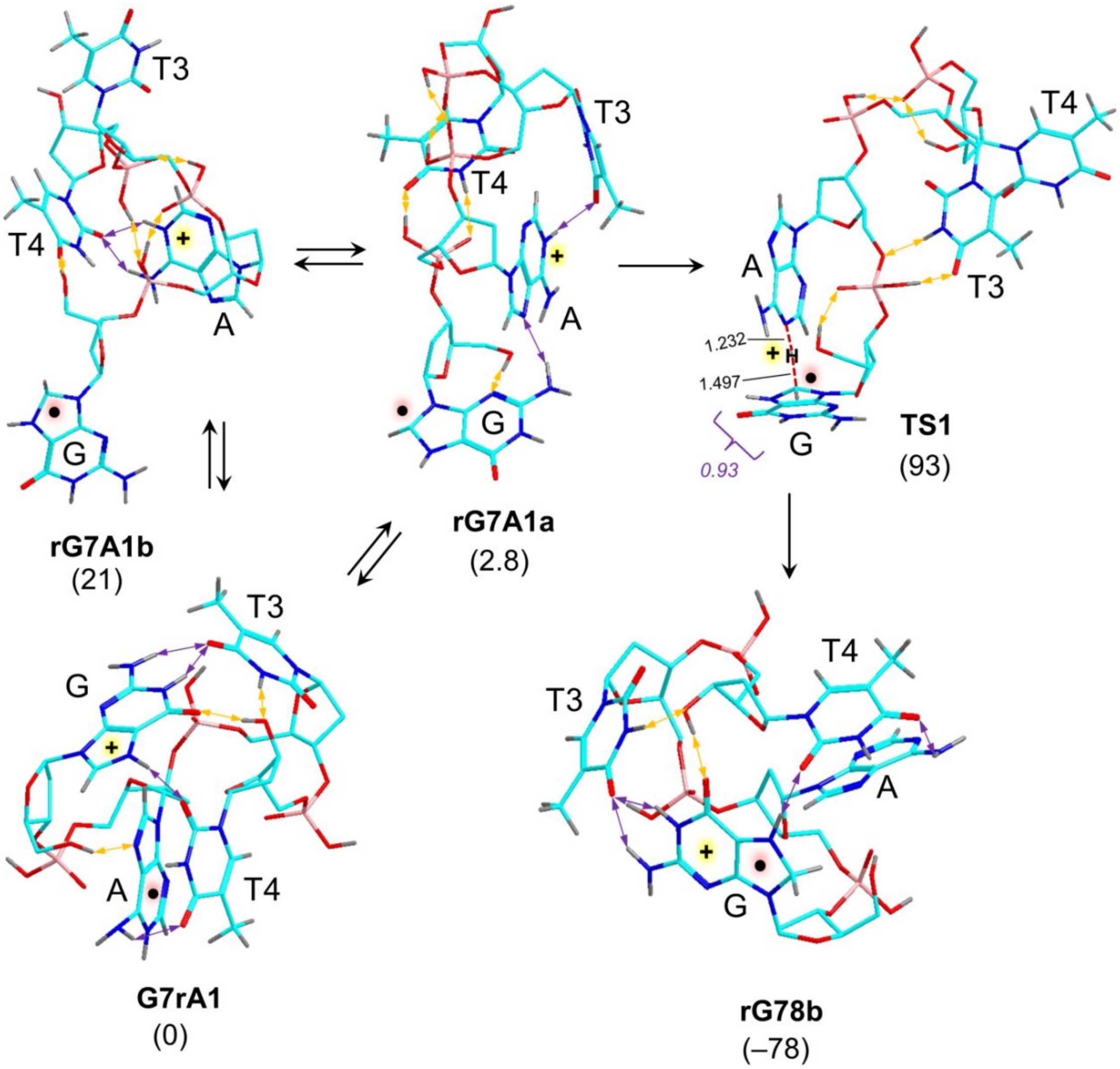

Scheme 2. Reactant and transition-state structures for hydrogen migration and exothermic isomerization of $(GATT+2H)^{+\bullet}$. Bond lengths (Å) and spin density in the guanine ring are shown for **TS1**. Relative energies (ΔH_0, kJ mol^{-1}) in parentheses.

Using the $k_{\mathrm{isom}}(E)$ in eq 9 indicated that for $k_{\mathrm{cool}} < 10^5$ s^{-1} the isomerization would still proceed with 99% efficiency, $x_{\boldsymbol{r}\mathbf{G78b}} \geq 0.99$, on the 0.15 s time scale. Previous estimates of k_{cool} ranged at $<10^4$ s^{-1},[70] suggesting that collisional cooling should be insufficient to prevent the isomerization of **G7rA1**. Efficient isomerization was also predicted by transition-state-theory (TST) kinetics for fully thermalized **G7rA1**. Fig. S4 (Supporting Information) indicates that for ion trap temperatures of >320 K the isomerization would be >99% complete. The facile isomerization was promoted by a low Arrhenius activation energy, E_a = 96.5 kJ mol^{-1}, and a high frequency factor of log A = 17.42. The latter was due to a positive entropy change for **G7rA1** → **TS1**, $\Delta S^{\ddagger}$ = 74-75 J mol^{-1} K^{-1} for the indicated temperature range. The **TS1** structure (Scheme 2) showed only a partial disruption of the dissociating adenine N-1–H bond at d(N–H) = 1.232 Å, consistent with an early transition state for the highly exothermic reaction. Population analysis indicated that 93% spin density was contained in the guanine ring in **TS1** (Scheme 2). At the same time, the **G7rA1** conformation in which T3 and T4 were hydrogen bonded to A and G refolded, resulting in a more open conformation of **TS1** and increasing its vibrational entropy.

An alternative pathway can be visualized as starting from the guanine radical **rG7A1a**, which is nearly isoenergetic with **G7rA1** (Table 2). Radical **rG7A1a** can undergo a proton transfer from the adenine N-1 position to the guanine C-8 via the same **TS1**. TST kinetic analysis under thermal conditions yielded E_a = 75.6 kJ mol^{-1} and log A = 13.51. Hence, this pathway had a lower activation energy but also a lower frequency factor than the one starting from **G7rA1**, which was consistent with a smaller rise of entropy in **TS1** ($\Delta S^{\ddagger}$ = 22-23 J mol^{-1} K^{-1} for the indicated temperature range). The temperature dependence (Fig. S4) indicated >95% isomerization at T > 330 K, which is within the range of ion-trap effective temperatures.[27,71-74]

We also considered an isomerization by hydrogen migration from thymine O-2 to guanine C-8 in the low-energy isomers **G7rT3** and **G7rT4** (Fig. 7) in which these nucleobases were in proximity. However, analysis of the potential energy surface along the presumed H-transfer trajectory indicated that it was associated with a disruption of strong hydrogen bonds of T4 to T3 and a phosphate (Fig. 7). For isomerization of **G7rT3,** this resulted in a substantial increase of potential energy. We located a transition state (**TS2**) for the isomerization of **G7rT4**, which was at 117 kJ mol^{-1} relative to **G7rT4** (Table 2, Scheme S1). TST rate constants for the reaction **G7rT4** → **TS2** were below 0.002 s^{-1} at 350 K (Fig. S5), indicating that this thymine radical would not undergo spontaneous isomerization upon storage in the ion trap. The RRKM rate constants for the **G7rT4** isomerization via **TS2** (Fig. 11b) were >3 orders of magnitude lower than those for **G7rT3**. Nevertheless, at a high excitation following electron transfer the population-averaged rate constant for **G7rT3,** $k_{2,\mathrm{isom}}(E) = 7.4 \times 10^{2}$ s^{-1}, indicated 0.9 ms lifetime for the radical. Collisional cooling was expected to have a substantial effect on the isomerization of **G7rT3.** For k_{cool} = 1000 s^{-1}, we calculated only 36% of **G7rT3** isomerizing to a guanine C-8 radical. It should be noted that the RRKM kinetics (Figure 11b) also indicated a large difference in the kinetic shifts for the isomerizations of **G7rA1** and **G7rT4**. The dissociations of **G7rA1** and **G7rT4** required 180 and 371 kJ mol^{-1} of excess internal energy above the respective TS in order to reach 50% conversion at 150 ms (Figure 11b).

Interestingly, the dissociation of (GATT+2H)$^{+\bullet}$ to $\boldsymbol{w_3}^+$ and $\boldsymbol{a_1}^\bullet$ that was observed upon CID and UVPD (Fig. 2) was calculated to have a relatively low threshold energy of 90 kJ mol^{-1} for **G7rA1** (Table 2), which was similar to the TS energy for the isomerization. However, the dissociation did not proceed spontaneously upon the exothermic electron transfer (Fig. 1a), despite the substantial vibrational excitation in the (GATT+2H)$^{+\bullet}$ formed (436 kJ mol^{-1}, *vide supra*). This may indicate that the phosphate elimination involved in the formation of the $\boldsymbol{w_3}^+$ ion had a substantial activation energy. Because of the fast isomerization of hot **G7rA1** or **rG7A1** to **rG78**, the more stable radical product was facing a substantially higher dissociation threshold (167 kJ mol^{-1}), resulting in a slow dissociation that was further limited by collisional cooling. Thus, fast isomerization of the primary **G7rA1** or **rG7A1** cation radicals, as predicted by RRKM calculations, was consistent with the observed stability of the (GATT+2H)$^{+\bullet}$ ions produced by highly exothermic electron transfer.

3.7. Comparison of tetranucleotide cation radicals

It was interesting to compare the structures and reactivity of (GATT+2H)$^{+\bullet}$ cation radicals vis-a-vis those of the related (GATC+2H)$^{+\bullet}$ tetranucleotide system.**[34]** In both systems, the primary cation radicals underwent exothermic isomerization by hydrogen migration to guanine C-8. However, in (GATC+2H)$^{+\bullet}$ the source of the hydrogen atom was the reduced 3'-cytosine radical whereas with (GATT+2H)$^{+\bullet}$ the H-atom originated from reduced adenine. The differences in the reduction sites in (GATC+2H)$^{+\bullet}$ and (GATT+2H)$^{+\bullet}$ can be seen as reflecting the different adiabatic recombination energies (RE_{adiab}) of the protonated nucleobases. These were calculated as $-RE_{adiab}$ = 4.54, 4.52, 5.25, and 5.52 eV for protonated N-1-H adenine, N-7-H guanine, N-3-H cytosine and O-4-H thymine cations, respectively (Table S12, Supporting Information). These figures are consistent with electron attachment to protonated cytosine in low-energy (GATC+2H)$^{2+}$ conformers where it led to a ground electronic state of the primary cytosine radical intermediate. In contrast, protonated thymine tautomers were energetically prohibitive in (GATT+2H)$^{2+}$ as indicated by the relative energies of **A1T3-4**, **G7T3-2**, and **G7T3-4** (Table 1) and thus were unlikely to be present as radical precursors. Electron attachment to a thymine ion tautomer would produce low-energy radicals **G7rT3**, and **G7rT4** (Table 2) which, however, were excluded by action spectra analysis. Electron attachment to protonated adenine or guanine nucleobases can be expected to be non-specific, judged by the very similar RE_{adiab} of the nucleobase ions (*vide supra*). The differences in the reduction sites in **G7rA1** on the one hand and **rG7A1a** and **rG7A1b** on the other, indicated a modulation of the nucleobase ion recombination energies depending on the charge and dipolar interactions created by the ion conformation. Similar effects have been reported for charge and dipole-guided electron attachment to peptide dications,**[75-77]** and ribonucleotide chimeras.**[31]** We note that effects on ionization energy of guanine stacking have been studied computationally, and the guanine ionization energies have been shown to decrease in artificially stacked dimers and trimers.**[78]** In contrast, effects on ionization or recombination energies of the DNA strand conformation have not been previously explored.

4. Conclusions

This combined experimental and computational study pointed to a spontaneous isomerization of $(GATT+2H)^{+\bullet}$ cation radicals when produced by one-electron reduction of $(GATT+2H)^{2+}$ dications in the gas phase. The primary reduction site, A or G, was determined by the protonation sites in the precursor dications that favored the basic adenine and guanine nucleobases. On the basis of action spectra, we concluded that the dominant final reduction product was a 7,8-dihydroguanine cation radical. Kinetic analysis of the reactants and transition states was interpreted as favoring a migration of adenine N-1-H to guanine C-8 that can proceed spontaneously at 320 K on the 0.15 s scale of ion storage and was substantially accelerated by internal excitation provided by highly exothermic electron transfer. Comparison of related tetranucleotide cation radicals, $(GATT+2H)^{+\bullet}$ and $(GATC+2H)^{+\bullet}$, both containing the 7,8-dihydroguanine cation-radical moiety, revealed differences in the reaction mechanisms for hydrogen atom migrations that were affected by the protonation sites as well as by the network of intramolecular hydrogen bonds in the reactants and transition states.

Conflicts of interest

There are no conflicts to declare.

Acknowledgments

Support from the Chemistry Division of the National Science Foundation (Grants CHE-1661815 and CHE-1624430) is gratefully acknowledged. F. T. thanks the Klaus and Mary Ann Saegebarth Endowment for general support.

References

(1) H.-A. Wagenknecht, Ed. Charge Transfer in DNA; Wiley-VCH: Weinheim, Germany, 2005; pp 1−23.

(2) M A. O'Neill and J. K. Barton, Sequence-Dependent DNA Dynamics: The Regulator of DNA-Mediated Charge Transport. In Charge Transfer in DNA; H. A. Wagenknecht, Ed.; Wiley-VCH: Weinheim, Germany, 2005; pp 27−31.

(3) C. J. Murphy, M. R. Arkin, Y. Jenkins, N. D. Ghatlia, S. H. Bossmann, N. J. Turro and J. K. Barton, *Science* 1993, 262, 1025.

(4) B. Giese, *Acc. Chem. Res*. 2000, **33**, 631.

(5) B. Giese, J. Amaudrut, A. K. Kohler, M. Spormann, and S. Wessely, *Nature* 2001, **412**, 318.

(6) A. K. Ghosh and G. B. Schuster, *J. Am. Chem. Soc*. 2006, **128**, 4172.

(7) J. Choi, S. Tojo, D.-S. Ahn, M. Fujitsuka, S. Miyamoto, K. Kobayashi, H. Ihee and T. Majima, *Chem. Eur. J.* 2019, **25**, 7711.

(8) J. Choi, D. W. Cho, S. Tojo, M. Fujitsuka and T. Majima, *J. Phys. Chem. A* 2015, **119**, 851.

(9) A. Kumar and M. D. Sevilla, *J. Phys. Chem. B* 2009, **113**, 11359.

(10) L. Rodriguez-Santiago, M. Noguera, J. Bertan and M. Sodupe, In *Quantum Biochemistry*, C. F. Matt, Ed.; Wiley-VCH: Weinheim, Germany, 2010; pp 219−242.

(11) J. Bertran, A. Oliva, L. Rodriguez-Santiago and M. Sodupe, *J. Am. Chem. Soc.* 1998, **120**, 8159.

(12) A. O. Colson, B. Besler and M. D. Sevilla, *J. Phys. Chem.* 1992, **96**, 9787.

(13) M. Hutter and T. Clark, *J. Am. Chem. Soc.* 1996, **118**, 7574.

(14) X. F. Li, Z. I. Cai and M. D. Sevilla, *J. Phys. Chem. B* 2001, **105**, 10115.

(15) X. F. Li, Z. I. Cai and M. D. Sevilla, *J. Phys. Chem. A* 2002, **106**, 9345.

(16) S. Steenken, *Chem. Rev.* 1989, **89**, 503.

(17) S. Steenken and S. V. Jovanovic, *J. Am. Chem. Soc.* 1997, **119**, 617.

(18) F. Tureček, *Top. Curr. Chem.* 2003, **225**, 77.

(19) L. Feketeova, B. Chan, G. N. Khairallah, V. Steinmetz, P. Maitre, L. Radom and R. A. J. O'Hair, *J. Phys. Chem. Lett.* 2017, **8**, 3159.

(20) R. C. Dunbar, *Int. J. Mass Spectrom.* 2000, **200**, 571.

(21) R. Antoine and P. Dugourd, *Lect. Notes Chem*. 2013, **83**, 93.

(22) N. C. Polfer and P. Dugourd, Eds. Laser Photodissociation and Spectroscopy of Mass Separated Biomolecular Ions. Lecture Notes in Chemistry; Springer: Cham, 2013; Vol. 83, pp 13−20.

(23) M. Lesslie, J. T. Lawler, A. Dang, J. A. Korn, D. Bím, V. Steinmetz, P. Maitre, F. Tureček and V. Ryzhov, *ChemPhysChem* **2017**, *18*, 1293.

(24) A. Dang, H. T. H. Nguyen, H. Ruiz, E. Piacentino, V. Ryzhov and F. Tureček, *J. Phys. Chem. B*, 2018, **122**, 86.

(25) A. Dang, Y. Liu and F. Tureček, *J. Phys. Chem. A* 2019, **123**, 3272.

(26) S. R. Huang, A. Dang and F. Turecek, *J. Am. Soc. Mass Spectrom.* 2020, **31**, in press. DOI: 10.1021/jasms.0c00095

(27) Y. Liu, A. Dang, J. Urban, and F. Turecek, *Angew. Chem, Int. Ed.* 2020, **59**, 7772.

(28) J. E. P. Syka, J. J. Coon, M. J. Schroeder, J. Shabanowitz and D. F. Hunt, *Proc. Natl. Acad. Sci. U. S. A.* 2004, **101**, 9528.

(29) K. Kobayashi and S. Tagawa, *J. Am. Chem. Soc*. 2003, **125**, 10213.

(30) K. Kobayashi, R. Yamagami and S. Tagawa, *J. Phys. Chem. B* 2008, **112**, 10752.

(31) J. A. Korn, J. Urban, A. Dang, H. T. H. Nguyen and F. Turecek, *J. Phys. Chem. Lett.* 2017, **8**, 4100.

(32) Y. Liu, J. A. Korn, A. Dang and F. Turecek, *J. Phys Chem. B* 2018, **122**, 9665.

(33) Y. Liu, J. A. Korn and F. Turecek, *Int. J. Mass Spectrom.* 2019, **443**, 22.

(34) S. R. Huang, Y. Liu and F. Turecek, *J. Phys Chem. B* 2020, **124**, 3505.

(35) S. G. Lias and J. E. Bartmess, Gas-Phase Ion Thermochemistry. In NIST Chemistry WebBook; P. J. Linstrom and W. G. Mallard, Eds; NIST Standard Reference Database Number 69, National Institute of Standards and Technology: Gaithersburg, MD, http://webbook.nist.gov (retrieved January-March 2020)

(36) A. Dang, J. A. Korn, J. Gladden, B. Mozzone and F. Tureček, *J. Am. Soc. Mass Spectrom.* 2019, **30**, 1558.

(37) C. J. Shaffer, R. Pepin and F. Tureček, *J. Mass Spectrom.* 2015, **50**, 1438.

(38) H. T. H. Nguyen, C. J. Shaffer, R. Pepin and F. Tureček, *J. Phys. Chem. Lett.* 2015, **6**, 4722.

(39) E. Viglino. C. J. Shaffer and F. Tureček, *Angew. Chem. Int. Ed.* 2016, **55**, 7469.

(40) H. J. Berendsen, J. V. Postma, W. F. van Gunsteren, A. R. H. J. DiNola and J. R. Haak, *J. Chem. Phys.* 1984, **81**, 3684.

(41) J. P. P. Stewart, *J. Mol. Model.* 2007, **13**, 1173.

(42) J. Řezáč, J. Fanfrlík, D. Salahub and P. Hobza, P. *J. Chem. Theory Comput*. 2009, **5**, 1749.

(43) J. P. P. Stewart, MOPAC 16. Stewart Computational Chemistry; Colorado Springs: CO, 2016.

(44) J. Řezáč, *J. Comput. Chem*. 2016, **37**, 1230.

(45) A. D.Becke, *Phys. Rev. A*. 1988, **38**, 3098.

(46) J. D. Chai and M. Head-Gordon, *Phys. Chem. Chem. Phys*. 2008, **10**, 6615.

(47) J. Tomasi, B. Mennucci and R Cammi, R. *Chem. Rev*. 2005, **105**, 2999.

(48) Y. Zhao and D. G. Truhlar, *Theor. Chem. Acc*. 2008, **120**, 215.

(49) A. E. Reed, R. B. Weinstock and F. Weinhold, *J. Chem. Phys*. 1985, **83**, 735.

(50) F. Furche and A. Ahlrichs, *J. Chem. Phys.* 2002, **117**, 7433.

(51) M. Barbatti, M. Ruckenbauer, F. Plasser, J. Pittner, G. Granucci, M. Persico and H. Lischka, *Wiley Interdiscip. Rev.: Comput. Mol. Sci.* 2014, **4**, 26.

(52) M. J. Frisch, G. W. Trucks, H. B. Schlegel, G. E. Scuseria, M. A. Robb, J. R. Cheeseman, G. Scalmani, V. Barone, G. A. Petersson, H. Nakatsuji, H. et al. Gaussian 16, Revision A03; Gaussian, Inc.: Wallingford, CT, 2016.

(53) R. G. Gilbert and S. C. Smith, *Theory of Unimolecular and Recombination Reactions*; Blackwell Scientific Publications, Oxford: 1990; pp. 52–132.

(54) L. Zhu and W. L. Hase, Quantum Chemistry Program Exchange; Indiana University: Bloomington (1994) Program no. QCPE 644.

(55) J. A. Gregersen and F. Tureček, *Phys. Chem. Chem. Phys.* 2010, **12**, 13434.

(56) K. K. Murray, *J. Mass Spectrom.* 1996, **31**, 1203.

(57) S. A. McLuckey, G. J. Van Berkel and G. L. Glish, *J. Am. Soc. Mass Spectrom.* 1992, **3**, 60.

(58) M. Sapunar, W. Domcke and N. Doslic, *Phys. Chem. Chem. Phys.* 2019, **21**, 22782.

(59) A. V. Tataurov, Y. You and R. Owczarzy, *Biophys. Chem.* 2008, **133**, 66.

(60) L. B. Clark, G. G. Peschel, and I. Tinoco, Jr., *J. Phys. Chem.* 1965, **69**, 3615.

(61) C. Marian, D. Noliting and R. Weinkauf, *Phys. Chem. Chem. Phys.* 2005, **7**, 3306.

(62) Y. Podolyan, L. Gorb and J. Leszczynski, *J. Phys. Chem. A* 2000, **104**, 7346.

(63) F. Tureček and X. Chen, *J. Am. Soc. Mass Spectrom.* 2005, **16**, 1713.

(64) C. Colominas, F. J. Luque and F. Orozco, *J. Am. Chem. Soc.* 1996, **118**, 6811.

(65) N. V. Hud and T. H. Morton, *J. Phys. Chem. A* 2007, **111**, 3369.

(66) A. Halder, S. Bhattacharya, A. Datta, D. Bhattacharyya and A. Mitra, *Phys. Chem. Chem. Phys.* 2015, **17**, 26249.

(67) R. R. Wu, B. Yang, G. Berden, J. Oomens and M. T. Rodgers, *J. Phys. Chem. B* 2014, **118**, 14774.

(68) A. Filippi, C. Fraschetti, F. Rondino, S. Piccirillo, V. Steinmetz, L. Guidoni and M. Speranza, *Int. J. Mass Spectrom.* 2013, **354-355**, 54.

(69) J.-Y. Salpin, S. Guillaumont, J. Tortajada, L. MacAleese, L. Lemaire and P. Maitre, *ChemPhysChem* 2007, **8**, 2235.

(70) R. Pepin and F. Tureček, *J. Phys. Chem. B* 2015, **119**, 2818.

(71) D. E. Goeringer and S. A. McLuckey, *J. Chem. Phys.* 1996, **104**, 2214.

(72) S. Gronert, *J. Am. Soc. Mass Spectrom*. 1998, **9**, 845.

(73) E. R. Lovejoy and R. R., Wilson, *J. Phys. Chem. A* 1998, **102**, 2309.

(74) W. A. Donald, G. N. Khairallah and R. A. J. O'Hair, *J. Am. Soc. Mass Spectrom.* 2013, **24**, 811.

(75) F. Turecek and R. R. Julian, *Chem. Rev*. 2013, **113**, 6691.

(76) C. L. Moss, T. W. Chung, J A. Wyer, S. B. Nielsen, P. Hvelplund and F. Turecek, *J. Am. Soc. Mass Spectrom.* 2011, **22**, 731.

(77) I. Anusiewicz, P. Skurski and J. Simons, *J. Phys. Chem. B* 2014, **118**, 7892.

(78) E. Cauet and J. Lievin, *Adv. Quant. Chem.* 2007, **52**, 121.

Figure Captions

Fig. 1. Electron-transfer dissociation mass spectra of doubly charged *m/z* 595 ions (a) $(GATT+2H)^{2+}$, and (b) $(AGTT+2H)^{2+}$. Insets show the peak profiles for charge-reduced ions.

Fig. 2. Tandem MS^3 spectra of $(GATT+2H)^{+\bullet}$ at *m/z* 1190. (a) CID-MS^3, (b) UVPD-MS^3 with 2 laser pulses at 250 nm. Ion relative intensities in both spectra are scaled to that of the most abundant ion as 100%.

Fig. 3. Tandem MS^3 spectra of $(AGTT+2H)^{+\bullet}$ at *m/z* 1190. (a) CID-MS^3, (b) UVPD-MS^3 with 3 laser pulses at 250 nm. Ion relative intensities in both spectra are scaled to that of the most abundant precursor ion as 100%.

Fig. 4. Photodissociation action spectra of $(GATT+2H)^{+\bullet}$ plotted as (a) sum of fragment ion relative intensities, (b) selected major and (c) minor dissociation channels.

Fig. 5. Photodissociation action spectra of $(AGTT+2H)^{+\bullet}$ plotted as (a) sum of fragment ion relative intensities, (b) selected major and (c) minor dissociation channels.

Fig. 6. ωB97X-D/6-31+G(d,p) optimized structures of low-energy $(GATT+2H)^{2+}$ dications. Atom color coding is as follows: cyan = C, red = O, blue = N, bronze = P, gray = H. Only exchangeable O-H, N-H and nucleobase hydrogen atoms are shown. Yellow double-headed arrows indicate hydrogen bonds involving backbone oxygens. Purple arrows indicate hydrogen bonds between the nucleobases. Relative free energies in kJ mol^{-1} are for gas-phase ions at 310 K.

Fig. 7. M06-2X/6-31+G(d,p) optimized structures of selected primary $(GATT+2H)^{+\bullet}$ cation radicals by electron attachment to dications. Atom color coding and hydrogen bonds as in Figure 6. Relative energies in parentheses (kJ mol^{-1}) are for gas-phase ions at 0 K.

Fig. 8. M06-2X/6-31+G(d,p) optimized structures of selected $(GATT+2H)^{+\bullet}$ cation radicals formed by hydrogen migration. Atom color coding and hydrogen bonds as in Figure 6. Relative energies in parentheses (kJ mol^{-1}) are for gas-phase ions at 0 K.

Fig. 9. M06-2X/6-31+G(d,p) calculated absorption spectra of (a) **rG78a** and (b) **rG78b**. Blue lines show vibronic spectra for 10 excited states spanning the wavelength region indicated by the brackets. Blue bands in the background are action spectra scaled to fit the oscillator strength range.

Fig. 10. Molecular orbitals involved in electron excitation to low excited states in **rG78b** (left panel) and **rG78a** (right panel). The wave function phases are distinguished by color. Excitation energies are from M06-2X/6-31+G(d,p) TD-DFT calculations.

Fig. 11. (a) Vibrational energy distribution, $P(E)$, in (black) the **G7A1a** dication precusor at 310 K and (red) **G7rA1** cation radical after exothermic electron transfer. (b) RRKM rate constants for the **G7rA1** (full circles) and **G7rT4** (empty triangles) isomerizations as a function of internal energy. Red arrows indicate the internal energies needed for log $k_{\mathrm{isom}} = 0.665$ to achieve 50% conversion at 150 ms.

Table 1. Relative energies of $(GATT+2H)^{2+}$ dications.

		Relative energy[a,b]		
Ion	Protonation sites	$\Delta H_{0,g}$	$\Delta G_{310,g}$[c]	$\Delta G_{310,aq}$[d]
G7A1a	G-N7, A-N1	0	0	5
G7A1b	G-N7, A-N1	14	1.7	15
G7A1c	G-N7, A-N1	14	16	0
G7A3a	G-N7, A-N3	39	19	29
G7A3b	G-N7, A-N3	43	28	42
A1T3-4	A-N1, T3-O4	39	33	52
G7T3-2	G-N7, T3-O2	44	16	24
G7T3-4	G-N7, T3-O4	76	64	86

[a] In kJ mol^{-1} for ωB97X-D/6-31+G(d,p) optimized strucutres. [b] Including B3LYP/6-31+G(d,p) zero-point vibrational energies scaled by 0.975 and referring to 0 K unless stated otherwise. [c] Relative free energies at 310 K. [d] Relative free energies from ωB97X-D/6-31+G(d,p) calculations including PCM solvation energies in the water dielectric.

Table 2. Relative energies of (GATT+2H)$^{+\bullet}$ cation radicals.

		Relative energy[a,b]	
Species/ reaction	Radical location	M06-2X[c] 6-31+G(d,p)	M06-2X[c,d] 6-311++G(2d,p)
G7rA1	A	0 (0)	0 (0)
rG7A1a	G	6.8 (6.4)	2.8 (2.4)
rG7A1b	G	34 (13)	21 (–1.1)
G7rT3	T3	–17 (–33)	–25 (–40)
A1rT3	T3	67 (50)	54 (37)
G7rT4	T4	–1.5 (–13)	–6 (–18)
rG78a	G	–112 (–125)	–120 (–132)
G7rA8	A	–89 (–98)	–94 (–104)
rG78b	G	–73 (–83)	–78 (–88)
rG78c	G	–40 (–49)	–78 (–88)
rA78	A	–45 (–45)	–47 (–46)
G7rA1→ TS1		111	93
G7rA1 → $w_3^+ + a_1^\bullet$		107 (44)	90 (27)
G7rT4→ TS2		123	117

[a]In kJ mol^{-1}. [b]Including B3LYP/6-31+G(d,p) zero-point vibrational energies scaled by 0.975 and referring to 0 K unless stated otherwise. [c]Relative free energies at 310 K in parentheses. [d]Single-point energy calculations on M06-2X/6-31+G(d,p) optimized geometries.

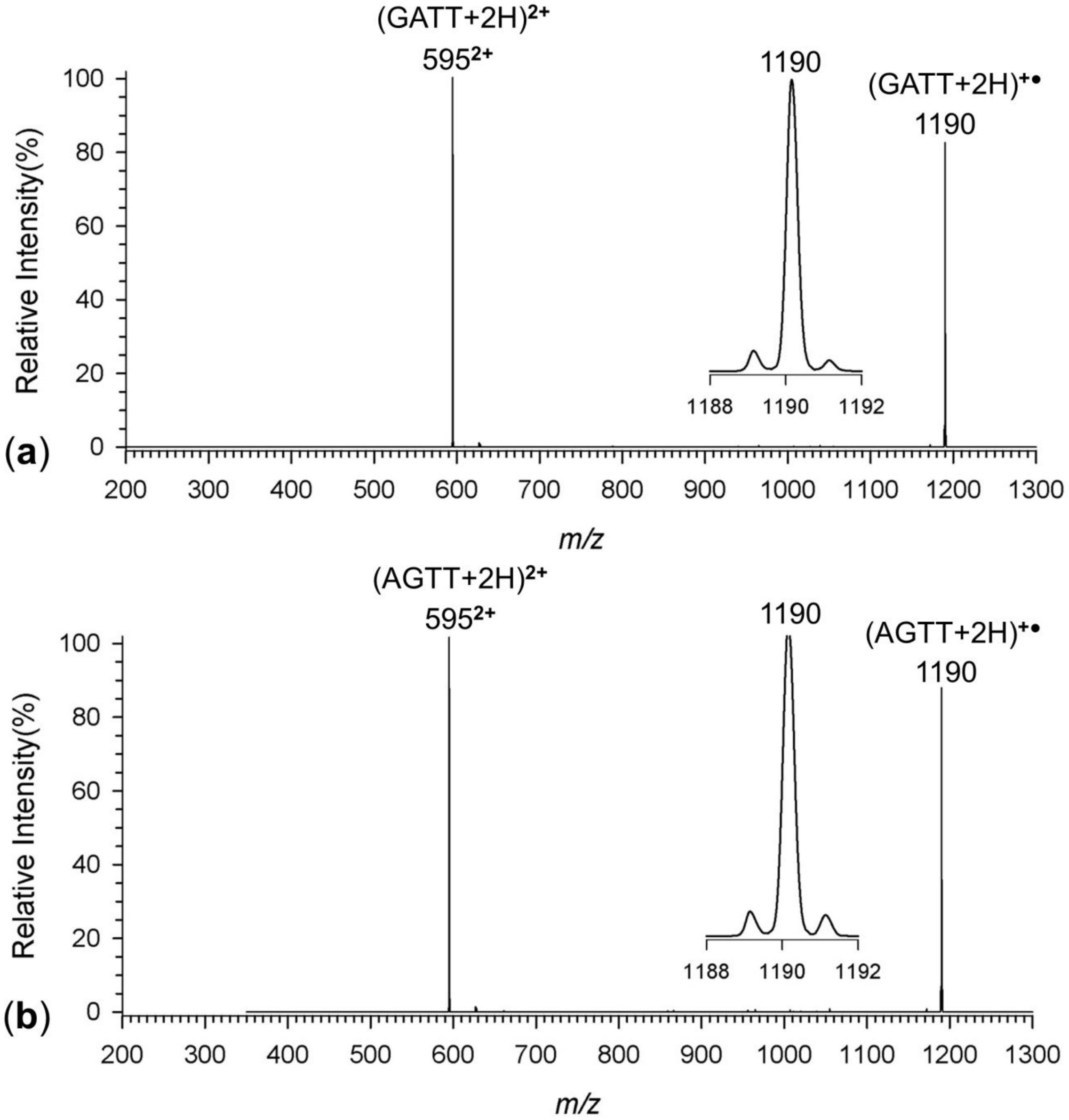

Fig. 1. Electron-transfer dissociation mass spectra of doubly charged *m/z* 595 ions (a) (GATT+2H)$^{2+}$, and (b) (AGTT+2H)$^{2+}$. Insets show the peak profiles for charge-reduced ions.

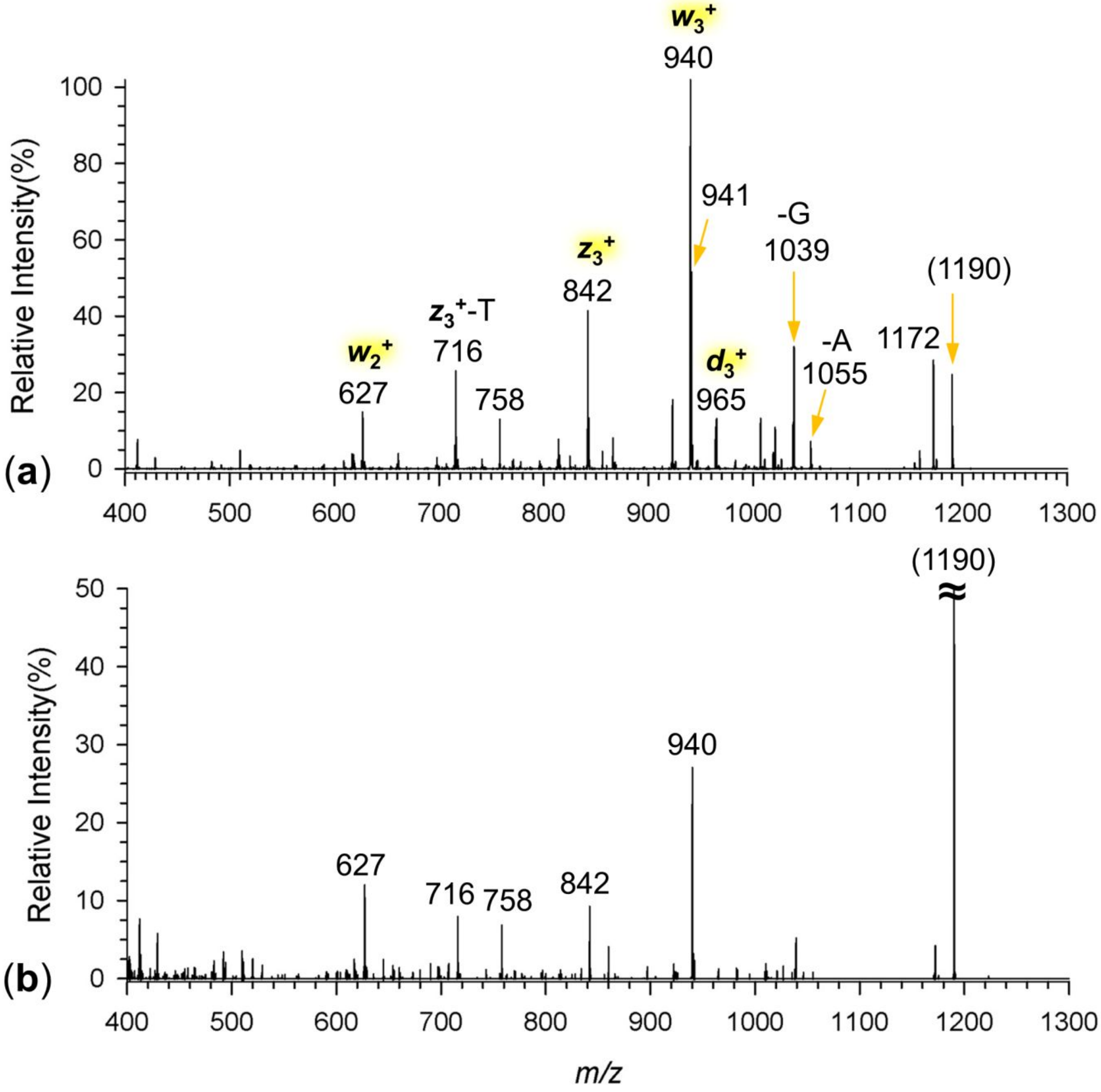

Fig. 2. Tandem MS^3 spectra of $(GATT+2H)^{+\bullet}$ at *m/z* 1190. (a) CID-MS^3, (b) UVPD-MS^3 with 2 laser pulses at 250 nm. Ion relative intensities in both spectra are scaled to that of the most abundant ion as 100%.

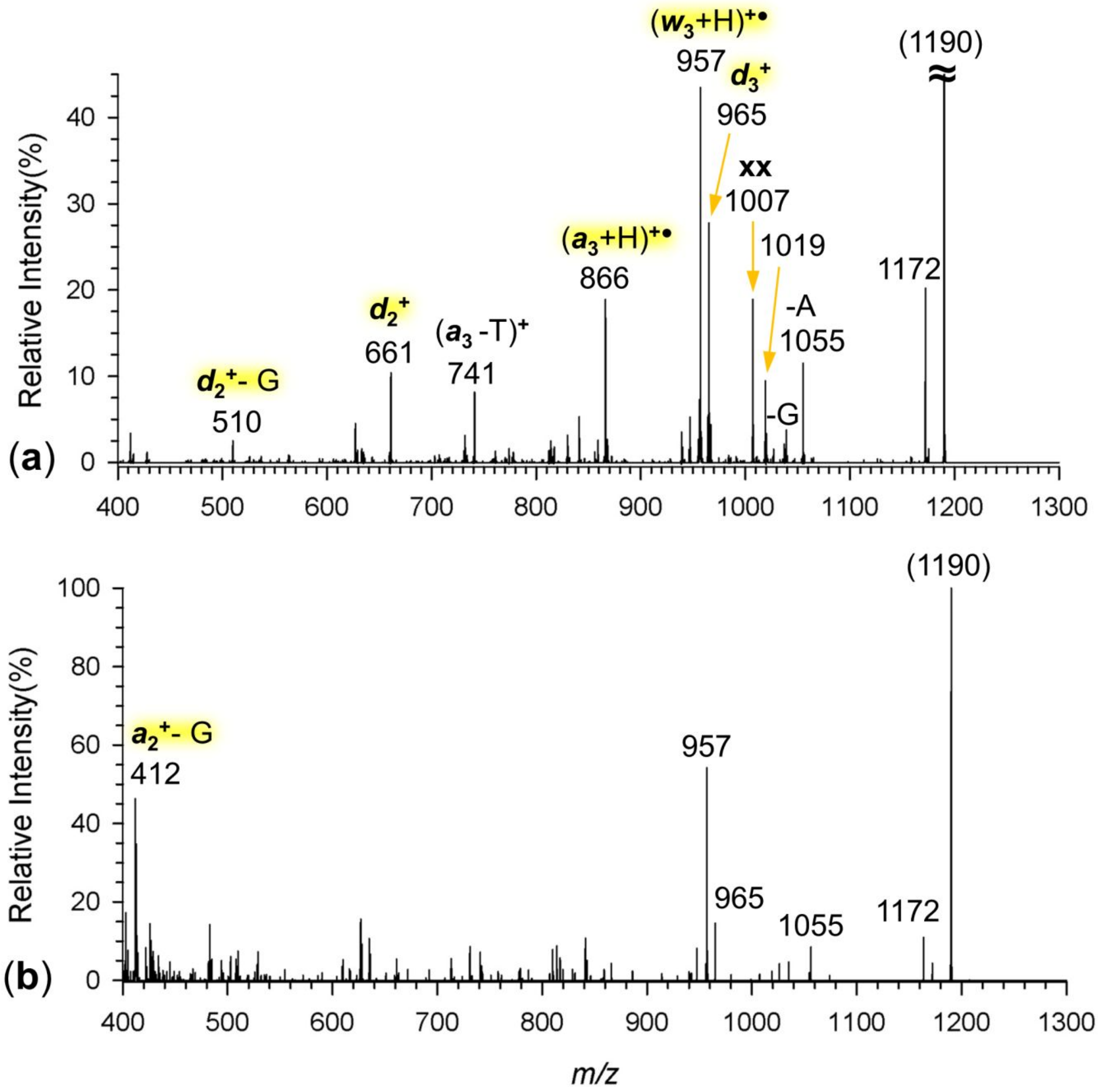

Fig. 3. Tandem MS^3 spectra of (AGTT+2H)$^{+\bullet}$ at *m/z* 1190. (a) CID-MS^3, (b) UVPD-MS^3 with 3 laser pulses at 250 nm. Ion relative intensities in both spectra are scaled to that of the most abundant precursor ion as 100%.

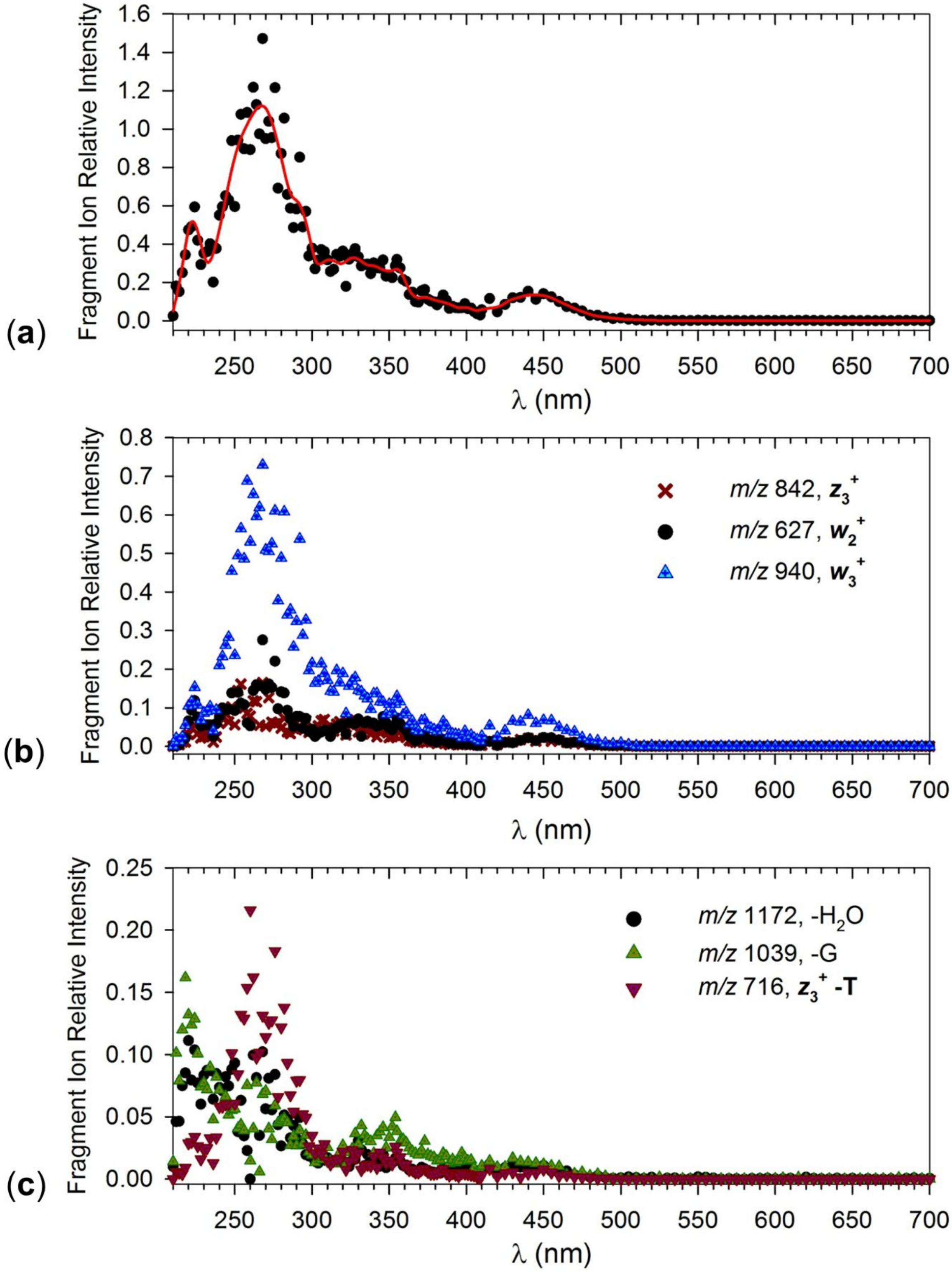

Fig. 4. Photodissociation action spectra of (GATT+2H)$^{+\bullet}$ plotted as (a) sum of fragment ion relative intensities, (b) selected major and (c) minor dissociation channels.

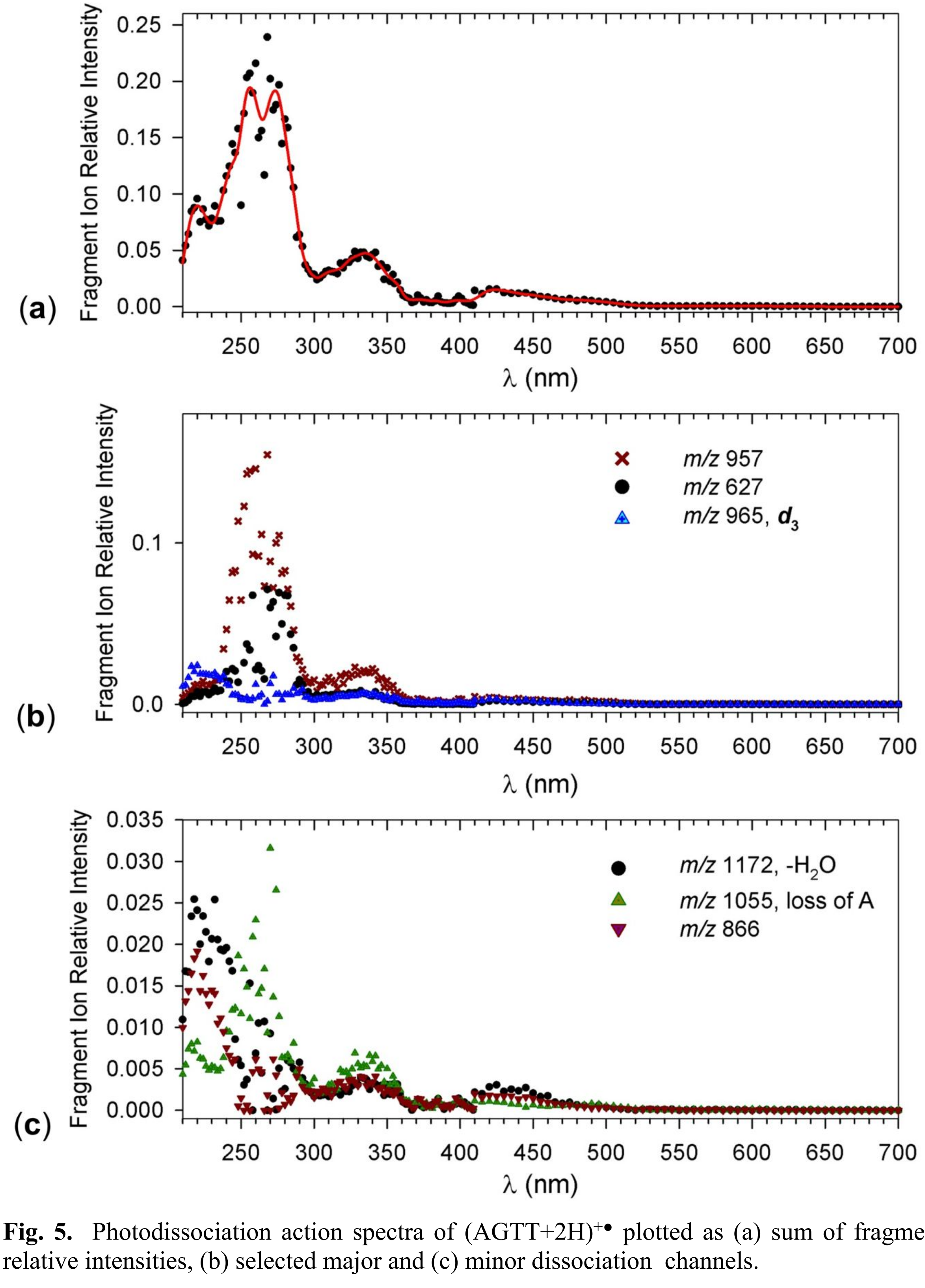

Fig. 5. Photodissociation action spectra of $(AGTT+2H)^{+\bullet}$ plotted as (a) sum of fragment ion relative intensities, (b) selected major and (c) minor dissociation channels.

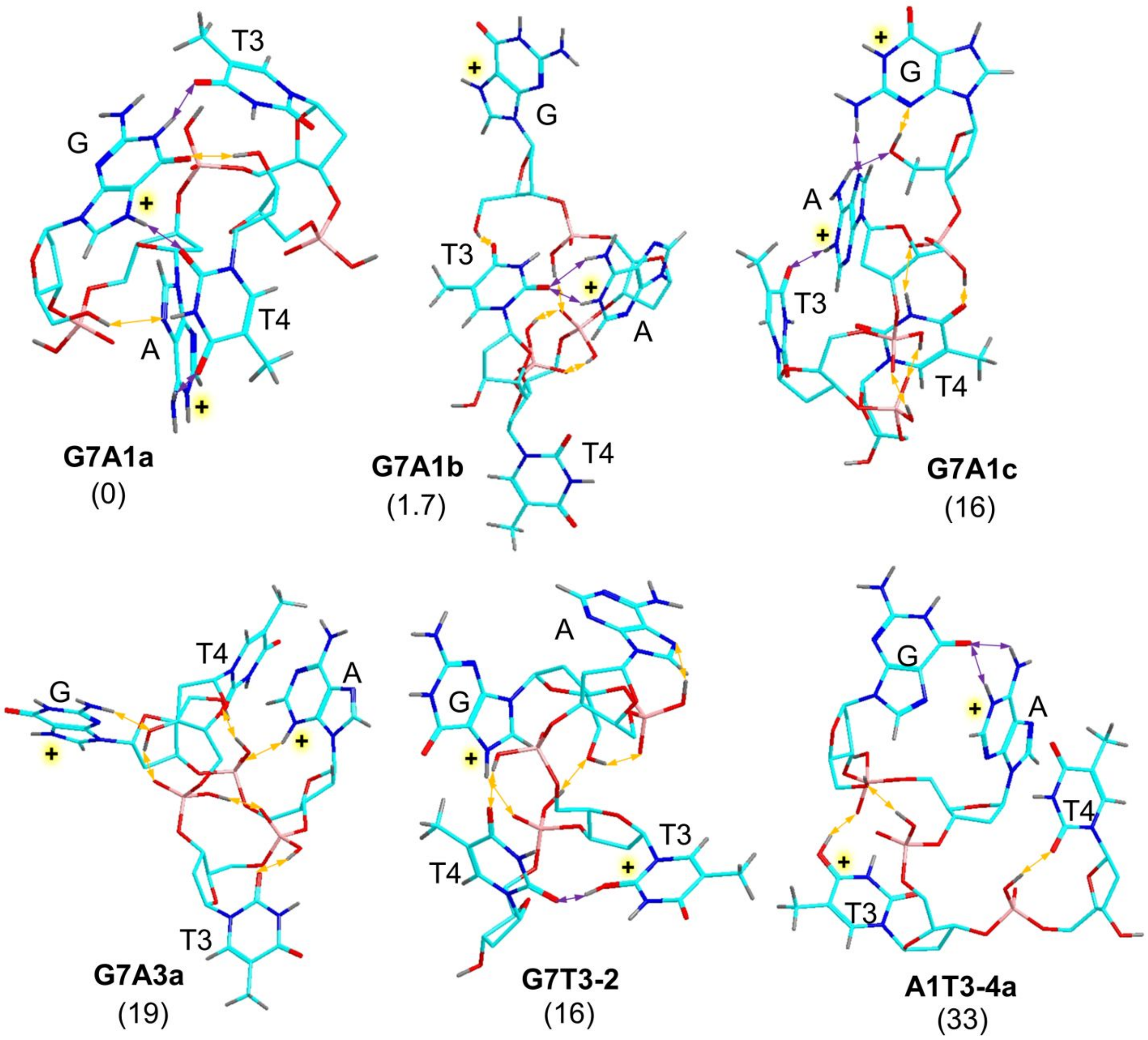

G7A1a
(0)

G7A1b
(1.7)

G7A1c
(16)

G7A3a
(19)

G7T3-2
(16)

A1T3-4a
(33)

Fig. 6. ωB97X-D/6-31+G(d,p) optimized structures of low-energy $(GATT+2H)^{2+}$ dications. Atom color coding is as follows: cyan = C, red = O, blue = N, bronze = P, gray = H. Only exchangeable O-H, N-H and nucleobase hydrogen atoms are shown. Yellow double-headed arrows indicate hydrogen bonds involving backbone oxygens. Purple arrows indicate hydrogen bonds between the nucleobases. Relative free energies in parentheses (kJ mol^{-1}) are for gas-phase ions at 310 K.

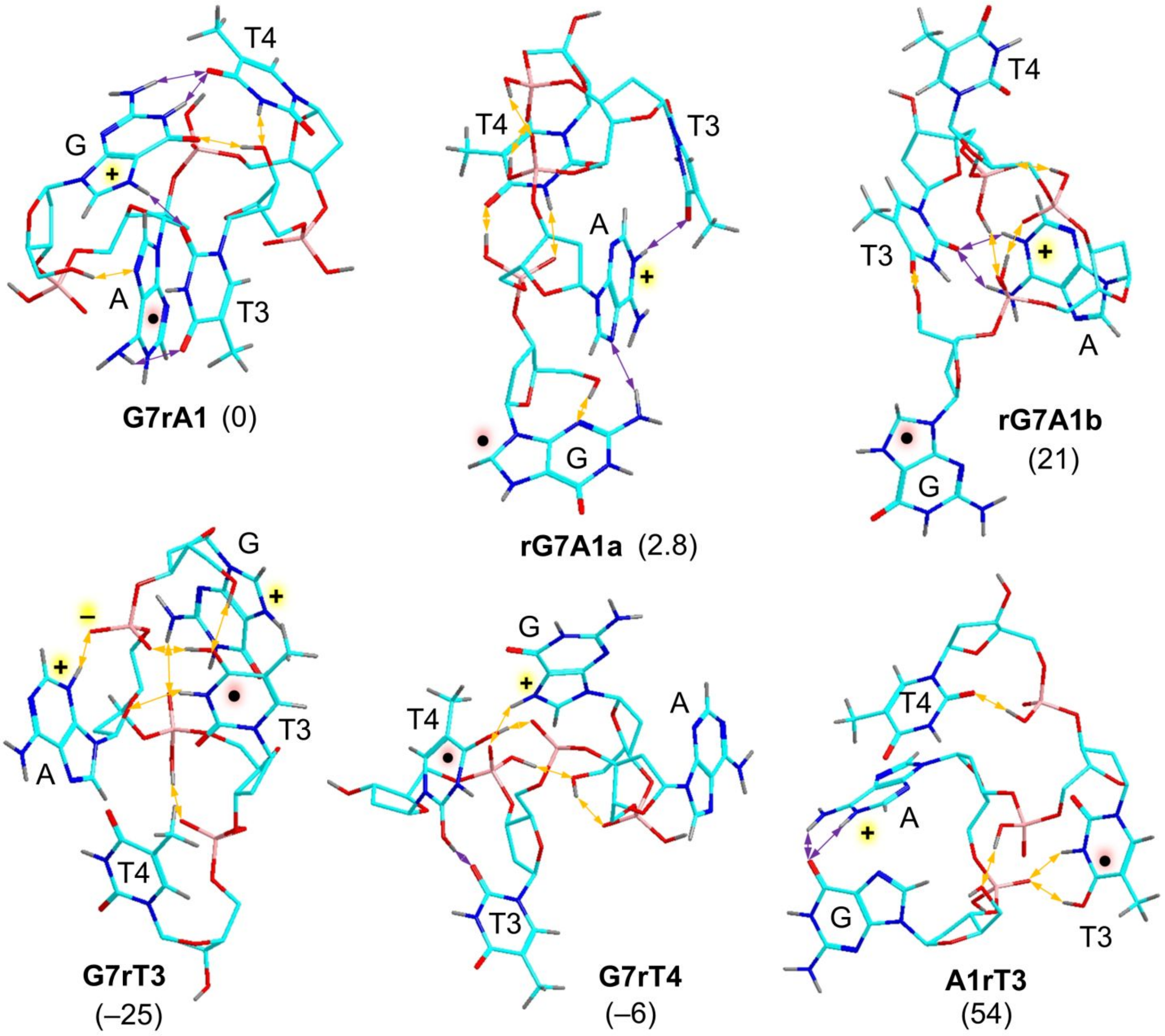

Fig. 7. M06-2X/6-31+G(d,p) optimized structures of selected primary $(GATT+2H)^{+\bullet}$ cation radicals by electron attachment to dications. Atom color coding and hydrogen bonds as in Fig. 6. Relative energies in parentheses (kJ mol^{-1}) are for gas-phase ions at 0 K.

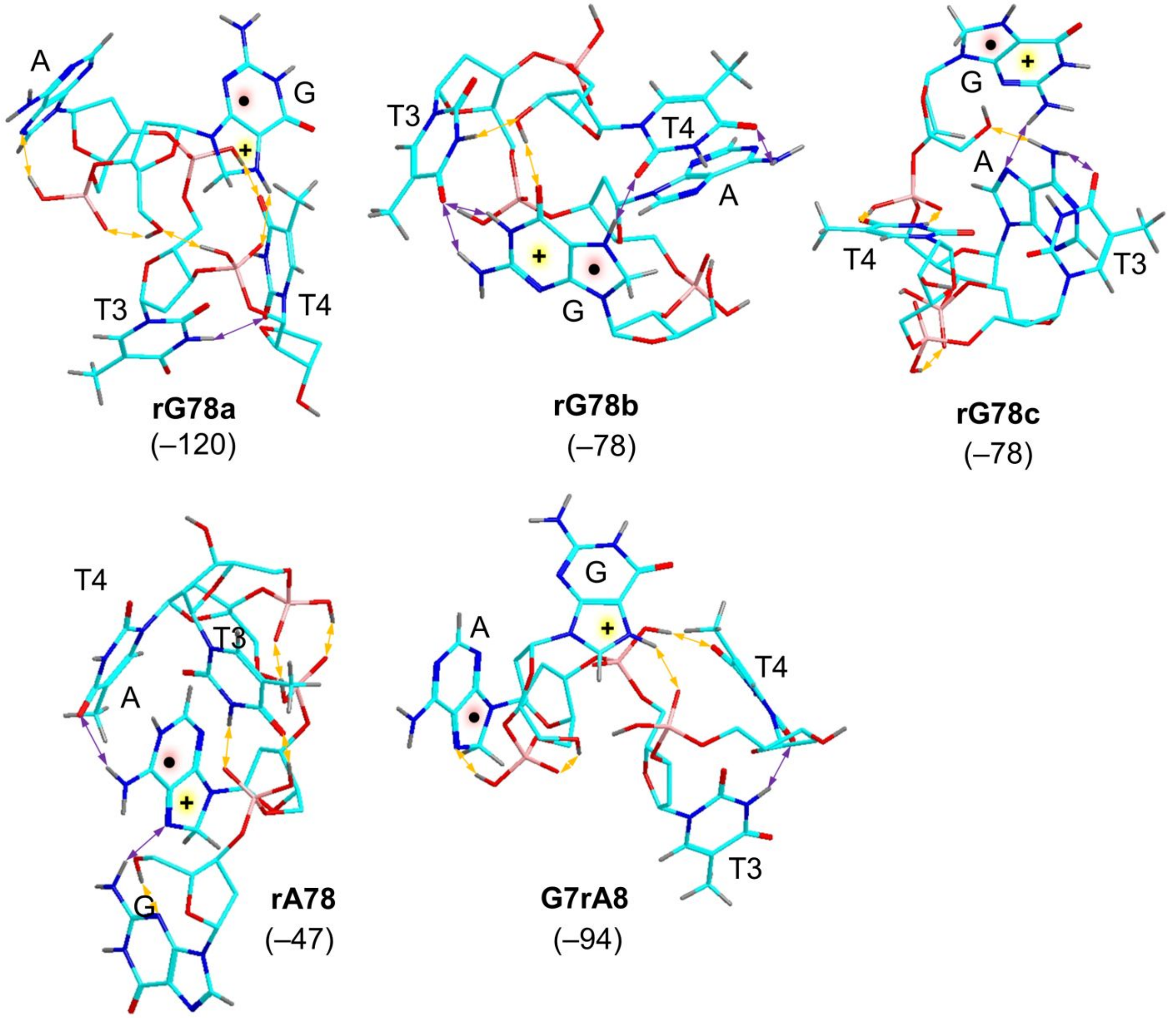

rG78a
(–120)

rG78b
(–78)

rG78c
(–78)

rA78
(–47)

G7rA8
(–94)

Fig. 8. M06-2X/6-31+G(d,p) optimized structures of selected (GATT+2H)$^{+\bullet}$ cation radicals formed by hydrogen migration. Atom color coding and hydrogen bonds as in Figure 6. Relative energies in parentheses (kJ mol^{-1}) are for gas-phase ions at 0 K.

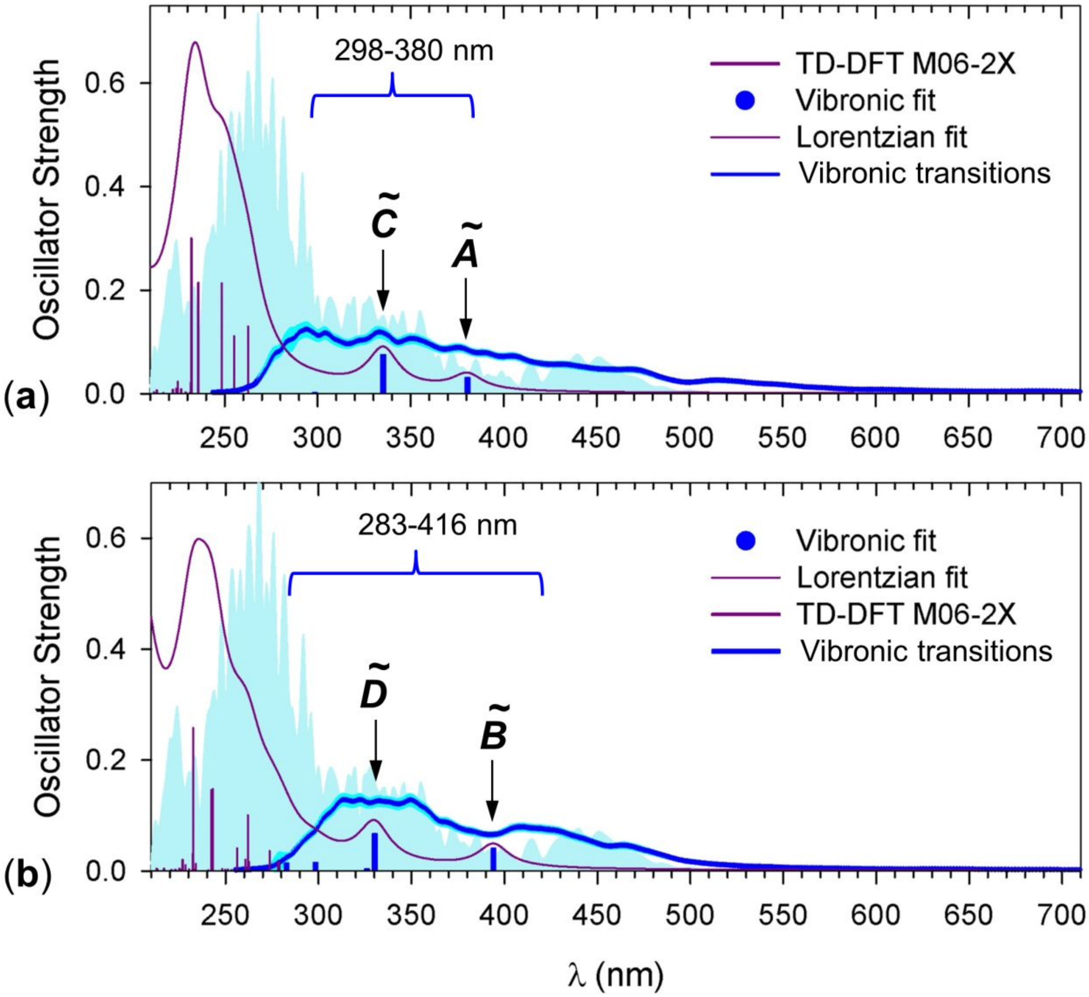

Fig. 9. M06-2X/6-31+G(d,p) calculated absorption spectra of (a) **rG78a** and (b) **rG78b**. Blue lines show vibronic spectra for 10 excited states spanning the wavelength region indicated by the brackets. Blue bands in the background are action spectra scaled to fit the oscillator strength range.

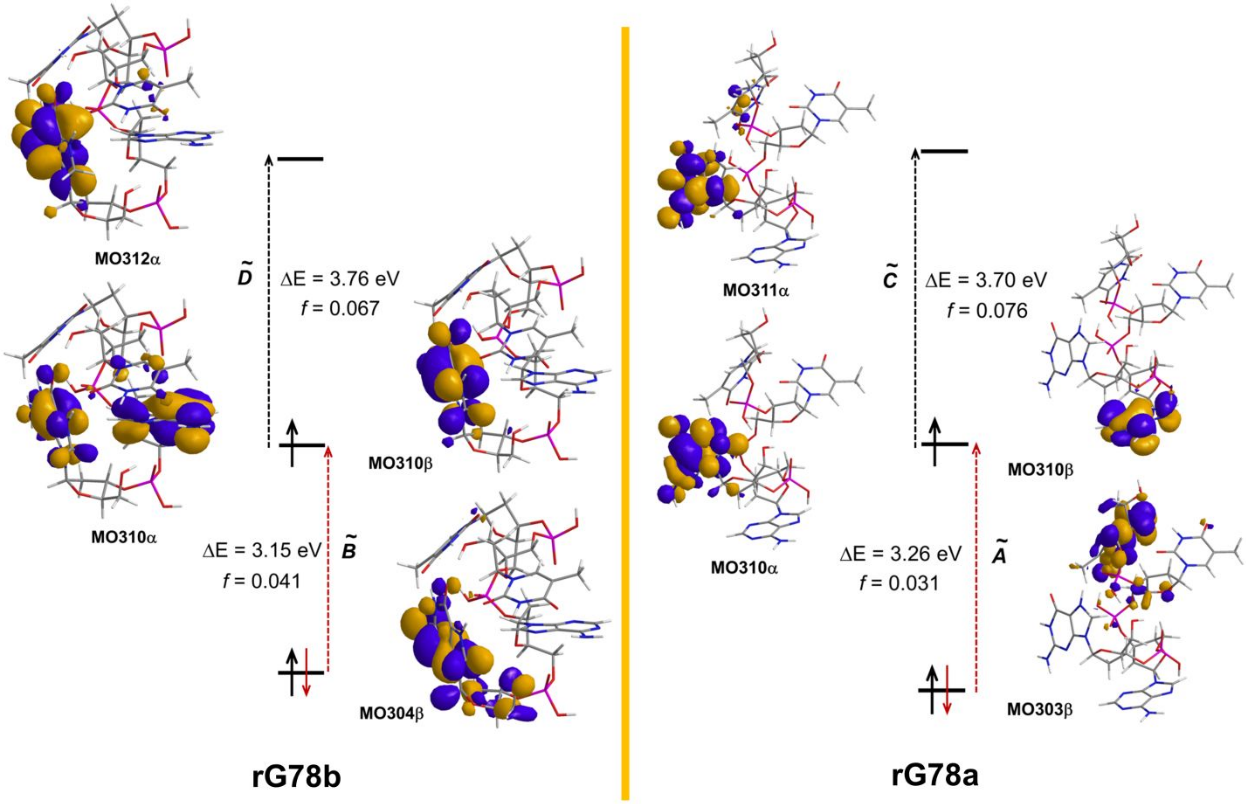

Fig. 10. Molecular orbitals involved in electron excitation to low excited states in **rG78b** (left panel) and **rG78a** (right panel). The wave function phases are distinguished by color. Excitation energies are from M06-2X/6-31+G(d,p) TD-DFT calculations.

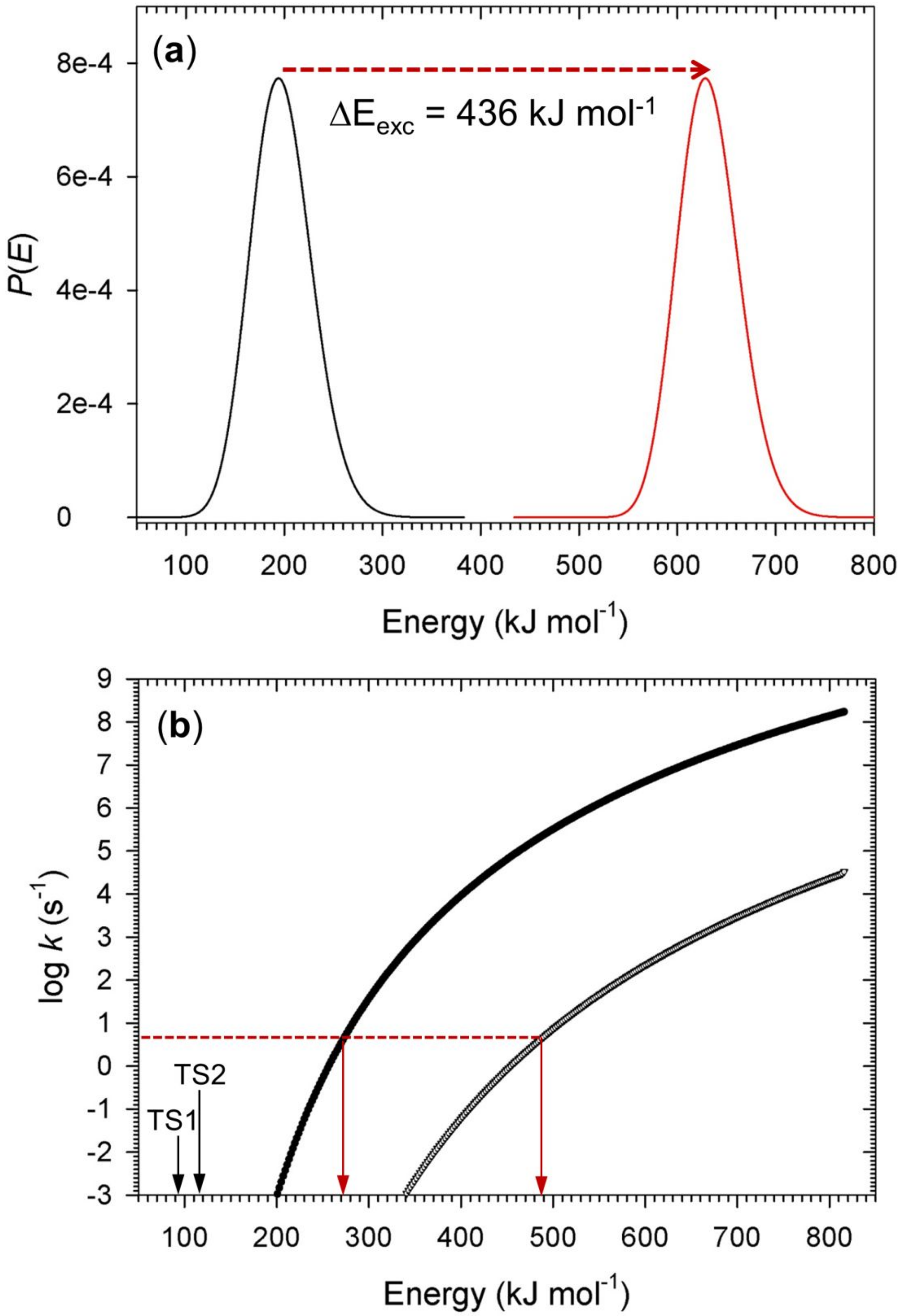

Fig. 11. (a) Vibrational energy distribution, *P*(*E*), in (black) the **G7A1a** dication precusor at 310 K and (red) **G7rA1** cation radical after exothermic electron transfer. (b) RRKM rate constants for the **G7rA1** (full circles) and **G7rT4** (empty triangles) isomerizations as a function of internal energy. Red arrows indicate the internal energies needed for log $k_{\mathrm{isom}} = 0.665$ to achieve 50% conversion at 150 ms.